Article

Not peer-reviewed version

A Novel Differentiated Control Strategy for Energy Storage System That Minimizes Battery Aging Cost Based on Multiple Health Features

Wei Xiao , Jun Jia * , Weidong Zhong , Wenxue Liu , Zhuoyan Wu , Cheng Jiang , Binke Li

Posted Date: 22 March 2024

doi: 10.20944/preprints202403.1129.v1

Keywords: energy storage station; lithium-ion battery; differentiated control; health feature; aging cost

Article

A Novel Differentiated Control Strategy for Energy Storage System That Minimizes Battery Aging Cost Based on Multiple Health Features

Wei Xiao [1], Jun Jia [2,*], Zhong Weidong [2], Liu Wenxue [3], Wu Zhuoyan [4], Jiang Cheng [2] and Li Binke [4]

[1] Department of Electrical Engineering, Tsinghua University, Beijing 100084, China; xiao-w20@mails.tsinghua.edu.cn
[2] Tsinghua Sichuan Energy Internet Research Institute, Chengdu 610042, China; zhongweidong@tsinghua-eiri.org (Z.W.); jiangcheng@tsinghua-eiri.org (J.C.)
[3] College of Mechanical and Vehicle Engineering, Chongqing 400044, China; wenxueliuu@cqu.edu.cn
[4] Science and Technology Research Institute, China Three Gorges Corporation, Beijing, 100038, China; wu_zhuoyan@ctg.com.cn (W. Z.); li_binke@ctg.com.cn (L. B.)
* Correspondence: jiajun@tsinghua-eiri.org

Abstract: In large-capacity energy storage systems, instructions are decomposed typically using an equalized power distribution strategy, where clusters/modules operate at the same power and durations. When dispatching shifts from stable single conditions to intricate coupled conditions, this distribution strategy inevitably results in increased inconsistency and hastened system aging. This paper presents a novel differentiated power distribution strategy comprising three control variables: the rotation status, the operating boundaries for both Depth of Discharge (DOD) and C-rates (C) within a control period. The proposed strategy integrates an aging cost prediction model developed to express the mapping relationship between these control variables and aging costs. Additionally, it incorporates the multi-colony particle swarm optimization (Mc-PSO) algorithm into the optimization model to minimize aging costs. The aging cost prediction model consists of three functions: predicting health features (HFs) based on the cumulative charge/discharge throughput quantity and operating boundaries, characterizing HFs as comprehensive scores, and calculating aging costs using both comprehensive scores and residual equipment value. Further, we elaborated on the engineering application process for the proposed control strategy. In the simulation scenarios, this strategy prolonged the service life by 14.62%, reduced the overall aging cost by 6.61%, and improved module consistency by 21.98%, compared with the traditional equalized distribution strategy. In summary, the proposed strategy proves effective in elongating service life, reducing overall aging costs, and increasing the benefit of energy storage systems in particular application scenarios.

Keywords: energy storage station; lithium-ion battery; differentiated control; health feature; aging cost

1. Introduction

Battery energy storage systems (BESSs) with varying capacities consist of several battery modules or clusters, each made up of multiple modules that further comprise individual cells[1]. Large-scale energy storage stations are usually equipped with numerous battery cabins corresponding to the installed capacity, and each battery cabin is formed by multiple clusters. The typical topology is illustrated in Figure 1.

 doi:10.20944/preprints202403.1129.v1

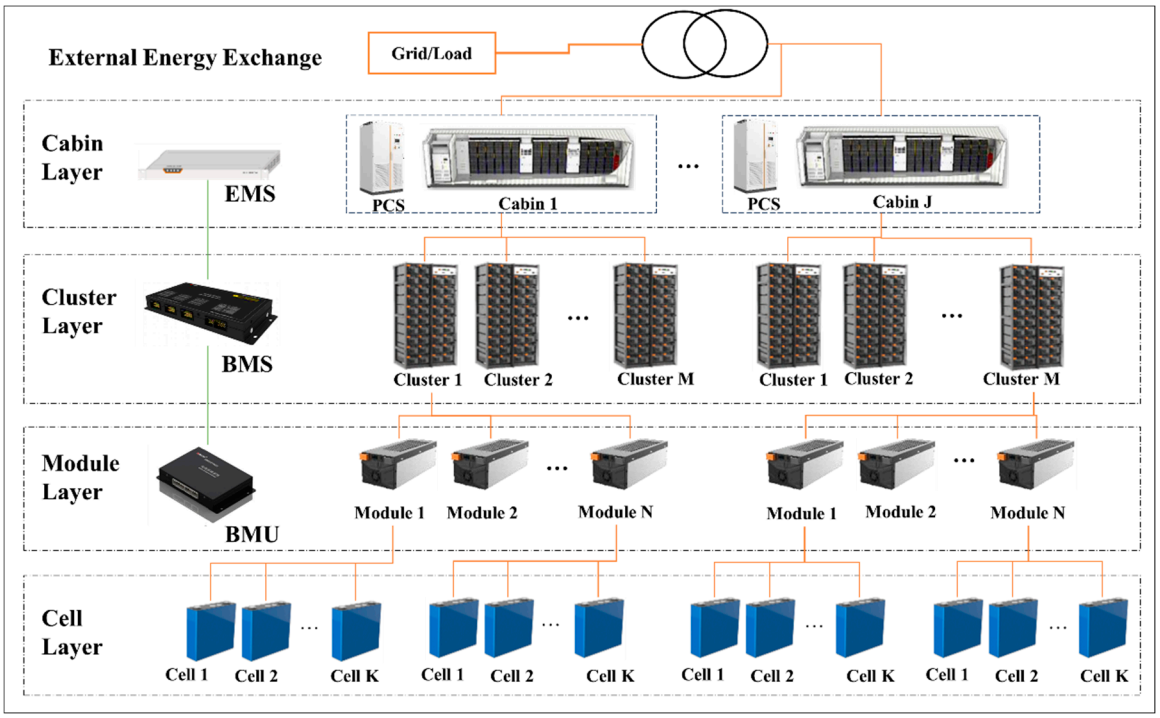

Figure 1. Typical topology of energy storage station.

Battery cabins typically receive dispatching instructions individually. Inside a cabin, control instructions are decomposed into clusters following the traditional control approach of equalized distribution, where all cells operate at the same power and durations. This dispatching method corresponds to a simplistic control system. However, due to inconsistencies among battery cells and modules[2], maintaining the same operational intensity exacerbates their inconsistency[3]. To enhance benefits, energy storage stations have evolved from traditional single-application scenarios to new composite application scenarios, resulting in a transition from stable single operating conditions—such as peak shaving, renewable energy consumption, and emergencies—to more intricate coupled operating conditions[4]. The inconsistency trend becomes more apparent in these new scenarios, due to the accelerated aging rate of "inferior batteries", thus adversely affecting the system's overall aging and safety[5]. As energy storage stations with inadequate integration during the early stages of the energy storage industry approach and surpass the halfway point of their service lives, coupled with the rising number of decommissioned batteries recycled for energy storage applications in recent years[6], the traditional equalized power distribution strategy is likely to pose progressively significant safety concerns.

Many scholars have studied control strategies for mitigating aging under power system scenarios. Zhao et al.[7] established the semi-empirical life model of the battery based on throughput, state of charge (SOC), and injected/output power of a BESS, applied to an aging rate equalization strategy for microgrid-scale battery energy storage systems. Xu et al.[8] developed a mapping relationship between system capacity losses and aging costs to optimize and support dispatching in the service market, ultimately boosting profits and prolonging battery longevity. However, energy storage systems were considered as a whole in the majority of previous research, primarily due to the unavailability of separate control over battery clusters/modules. In the traditional topological structure shown in the cabin layer of Figure 1, one power conversion system (PCS) corresponds to one battery cabin, where power is simply distributed to clusters and modules in an equalized manner. Ci et al.[9]proposed the dynamic reconfigurable battery energy storage technology. In comparison to the conventional norm of fixed series-parallel connections, the DRB networks use new program-controlled connections between battery cells/modules.

Limited literature explores differentiated control modes in the context of batteries. Yan et al.[10] primarily concentrated on investigating the impact of DOD, establishing a control strategy for

 doi:10.20944/preprints202403.1129.v1

frequency regulation scenarios aimed at enhancing battery lifetimes. Furthermore, Karunathilakeet al.[11] developed a multi-objective optimization control strategy that takes into account aging and is based on multiple features reflecting energy and power performance. However, They focused on multiple independent cells as the subjects of research. These studies emphasized the State of Health (SOH) as the primary optimization objective, rather than considering the enhancement of overall operational performance. According to the findings of the literature[12], with the increasing complexity of energy storage conditions in power system applications and the coupled and variable aging mechanisms, additional health indicators are essential for assessing the performance of energy storage systems.

In conclusion, implementing a differentiated control strategy for battery systems that consider the combined influence of multiple HFs is crucial to efficiently address inconsistency amplification and extend service life. In Section 2, the primary algorithm and its application process are introduced. In Section 3, the experiment is detailed, and both the multi-dimensional HFS extraction method and the prediction technique are introduced. In Section 4, the mapping of aging costs is delineated, incorporating comprehensive scoring and health status. Finally, a simulation comparison is presented for an industrial park scenario in Section 5.

2. Control Strategy

2.1. Optimization Control Strategy to Minimize Aging Cost in a Single Operational Period

Optimization control can be applied to physical objects like battery clusters, a battery cluster, a battery module, or multiple cells. To simplify the discussion process, multiple clusters are considered as the independently controlled objects to elucidate optimization control below. The rotation status (RS) of all battery clusters and their operating boundaries are determined within an operational period, aiming to minimize the predicted aging cost through optimization. The framework of the optimization algorithm is shown in Figure 2:

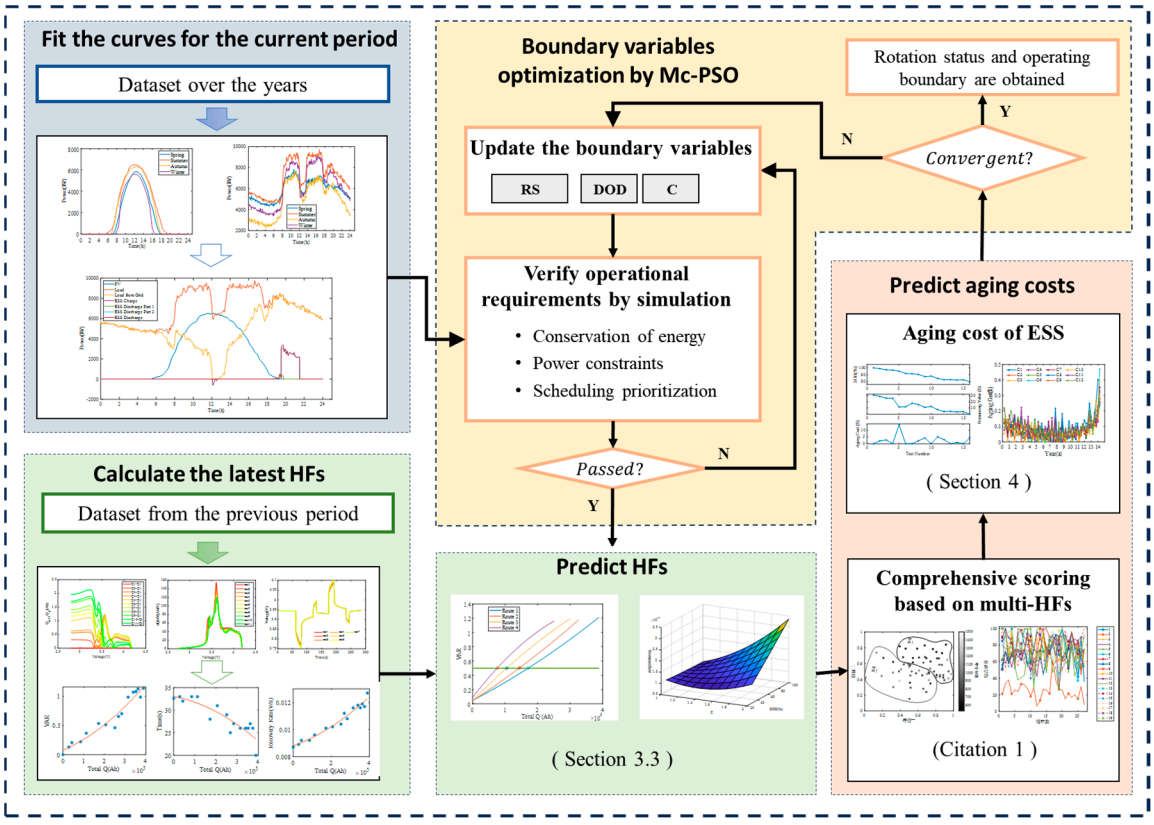

Figure 2. Framework of optimization algorithm.

 doi:10.20944/preprints202403.1129.v1

A period of time with similar conditions is defined as a study period. Input data collected over this period across multiple years is utilized to create a typical dispatching curve with the latest data gathered and through a fitting process. By employing boundary parameters that ensure effective responses to dispatching instructions, multiple HFs are predicted at the end of an operational period. Subsequently, a comprehensive score is calculated to evaluate aging costs. The Mc-PSO algorithm is then utilized to adjust control variables until operating boundaries are identified that lead to the lowest aging cost.

The optimization model is described as follows:

Optimization objective: minimize predicted aging cost in current period.

$$\min \sum_{1}^{M} C_{aging,m}^{pre} \tag{1}$$

Where, m denotes the number of clusters within one battery cabin, taken as m=1, 2, ⋯, M; $C_{aging,m}^{pre}$ denotes the predicted aging cost of cluster m.

The constraints are as follows:

The most important constraint is to ensure that performance does not fall below the expectation. Specifically, the execution of dispatching instructions signals the realization of anticipated performance. In simulation operations, the completion of the most rigorous instructions serves as the benchmark, forming the verification module for simulation operations as illustrated in Figure 2. In addition, it is assumed that no rigorous instructions would remain unfulfilled in real dispatching, based on the principle of negotiating the dispatchable range with the upper-level dispatching system by the EMS of energy storage stations one day in advance: The State of Power (SOP) upper limits reported by EMS would be acknowledged by the upper-level dispatching system, and dispatching curve instructions issued from the upper-level system would not surpass the reported upper limits.

The accumulated maximum available power $P_{m,t}^{avail}$ of all battery clusters at any given time (t) is greater than or equal to the dispatching power required to be responded by the corresponding battery cabin.

$$\sum_{1}^{M} P_{m,t}^{avail} \geq P_{j,t}^{demand}, t \in N \tag{2}$$

Where, j denotes the battery cabin number, taken as j=1, 2, ⋯, J, indicating the number of battery cabins at an energy storage station.

The maximum power does not exceed the C-rate boundary C_m^{limit} obtained from a solving process:

$$\left| P_{m,t}^{avail} \right| \leq C_m^{limit} \bullet P_{rated} \tag{3}$$

Where, P_{rated} denotes the rated power at a C-rate of 1C.

SOC_m^{min} is constrained by DOD boundaries:

$$SOC_m^{min} \geq SOC_m^{max} - DOD_m^{limit} \tag{4}$$

SOC_m^{max} denotes the maximum State of Charge (SOC) value after charging, generally taken as 100%, to ensure that the energy storage station can serve for emergencies in most cases. SOC is subjected to correction using the ampere-hour integral method:

$$SOC_{t+1} = SOC_t - I_t \bullet \Delta t / Q_0 \tag{5}$$

 doi:10.20944/preprints202403.1129.v1

Where, I_t denotes the effective value of current at a given time (t), with a positive value indicating discharge and a negative value indicating charge. Δt denotes the time interval and Q_0 denotes the rated capacity.

The simulation scenarios in this paper involve SOC calculations based on data with high precision and granularity, to ensure the SOC is error-free. However, SOC may be corrected in engineering applications, following suggestions given in the authors' previous articles[13].

The operational process fulfill the law of energy conservation:

$$\left(Q_{PV}-Q_{Load}^{PV}+Q_{Grid}^{charge}\right)\bullet\eta=Q_{Load}^{Bat} \tag{6}$$

Where, Q_{PV} denotes the power generation from photovoltaic (PV); Q_{Load}^{PV} denotes the power consumption of loads from direct PV supply; Q_{Grid}^{charge} denotes the power energy of the energy storage system by charge from the grid; η denotes the battery discharge efficiency; and Q_{Load}^{Bat} denotes the power supply from batteries to loads.

DOD^{limit} and C^{limit} operating boundaries are the variables to be optimized. However, each battery cluster covers the whole optional range, resulting in an intricate solving process. To reduce the solving difficulty and control complexity, the following two methods are applied for simplification. The first method involves taking C values as 0.25, 0.5, ⋯, 1.75 and 2, and DOD as discrete points of 20%, 30%, ⋯,100%, to simplify the solution domain space dimensionality. The second method is to introduce a new variable, Rotation Status in operation, to preliminarily define the range of boundary parameters and narrow the search scope. RS includes stable operation (*S*), dynamic operation (*D*), and emergency operation (*E*). Each rotation status imposes specific constraints on the maximum values of the operating boundaries, as outlined in Table 1.

Table 1. Correlation between rotation status and operating boundaries.

	S	*D*	*E*
DOD_{max}^{limit}	D1	D2	D3
C_{max}^{limit}	C1	C2	C3

Where, D1>D2>D3, C1<C2<C3. For instance, when a high C value is used for emergency operation (*E*), it is crucial to limit DOD to prevent the undervoltage of certain cells at a low SOC.

Moreover, the rotation status influences the priority of power distribution. The priorities, based on ΔC (absolute value of C-rate change between two scheduling time intervals), are presented below:

$$\begin{cases} S_1 > E > D > S_0, \Delta C \geq Ca \\ S_1 > D > S_0 > E, \Delta C \in (0,\ \ Ca] \\ E > D > S, \Delta C < 0 \end{cases} \tag{7}$$

Where, S_1 represents the steady-state operating battery that has been started, and S_0 represents those that have not been started. *Ca* indicates threshold to determine significant power changes, generally taken as C^{limit} of *E*.

The general principle is to minimize the frequency of startups by preventing inactive batteries from being enabled frequently. In the case of load increasing, S_1 batteries are raised first up to the maximum permissible power. If the demand cannot be satisfied, *D* batteries take precedence to respond if they remain in operation, before enabling other *S* batteries. During load shedding, *E* and *D* batteries are successively reduced in priority for transition into standby mode.

The following additional operating rules are followed:

(1) In the case of emergency batteries enabled, when other batteries are sufficient to take the place of *E* batteries, they will be reduced in power at a rate of 2%/s for transition into standby mode.

 doi:10.20944/preprints202403.1129.v1

(2) If other batteries reach the lower limit of DOD, *D* and *E* will be enabled to fill the vacancy successively, to meet the requirements of charging and discharging instructions.

Solving method:

The initial values of RS, DOD^{limit} and C^{limit} generally follow the values in the previous operational period to further speed up the solving process. The reasons include: (1) There is not much difference between the dispatching curves in two consecutive periods. (2) Aging costs arising from changes in HFs increase slowly under circumstances without safety concerns.

The Mc-PSO algorithm is used for solving and its introduction is omitted in this paper as it has been thoroughly explained in the authors' previous literature[14].

2.2. Rolling Optimization Process for Long-Time Operational Scenarios

Under the constraints of boundary parameters and adhering to actual dispatching curves, the ultimate aging levels of battery packs typically do not match the predicted values precisely. However, the relative magnitude relationship among the aging levels closely mirrors the predictions. To eliminate the estimation errors of HFs after long-term operation, a rolling optimization process is proposed. The energy management system (EMS), integrated with this strategy at energy storage stations, performs periodic control based on boundaries derived from the solving process. Following each period, the multi-dimensional HFs are updated using actual operational data, serving as the algorithm's initial input for the next period. The proposed strategy contributes to minimizing the total aging cost of energy storage systems after extended operational durations, as shown in Figure 3.

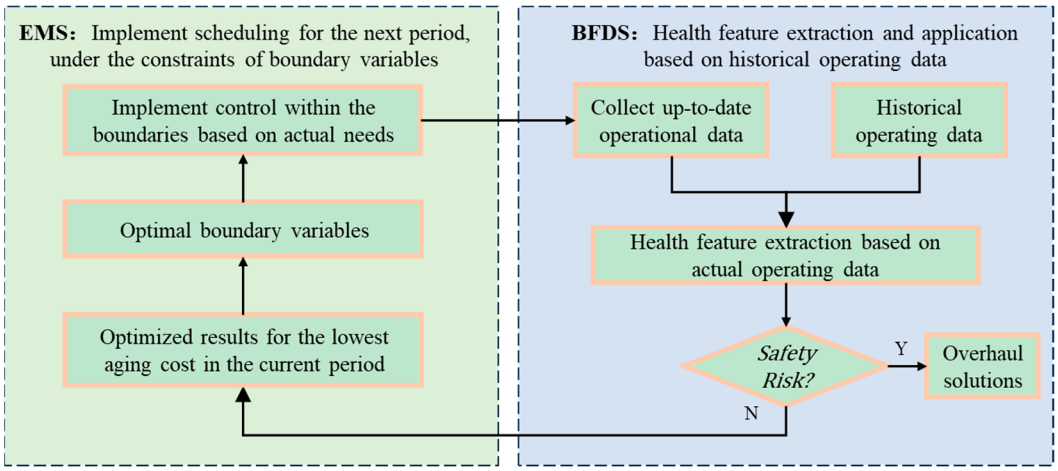

Figure 3. Application process based on EMS and BFDS.

At the end of each operational period, actual data are imported into the battery fault diagnosis system (BFDS) specially developed for energy storage stations, as shown in Figure 4. The platform developed by the author's team spending over two years integrates multiple functional modules for energy storage stations, such as operational data preprocessing, fault diagnosis, health assessment, and inconsistency analysis. BFDS extracts real HFs as input for a new period and identifies any safety concerns based on these HFs. Any safety concerns identified lead to the suspension of control to initiate the inspection and maintenance process.

The key HFs to be considered include the "capacity diving" risk[15], temperature rise rate[16], and internal short-circuit resistance[17], all of which are strongly linked to the risk of thermal runaway[18]. When safety risks escalate, batteries are prone to exhibiting "capacity diving." The predictive method has been proposed in the authors' previous papers[19]. Other common fault diagnosis studies can also be found in the previous related articles[20,21]. If a HF deteriorates but is not yet sufficient to cause safety accidents, the aging costs will sharply rise due to the significant decrease in comprehensive scores, leading to stricter control constraints. This mechanism helps to

 doi:10.20944/preprints202403.1129.v1

integrate safety into the control strategy to some extent. In the absence of any hidden dangers identified, the solving process for optimization control in subsequent periods is initiated.

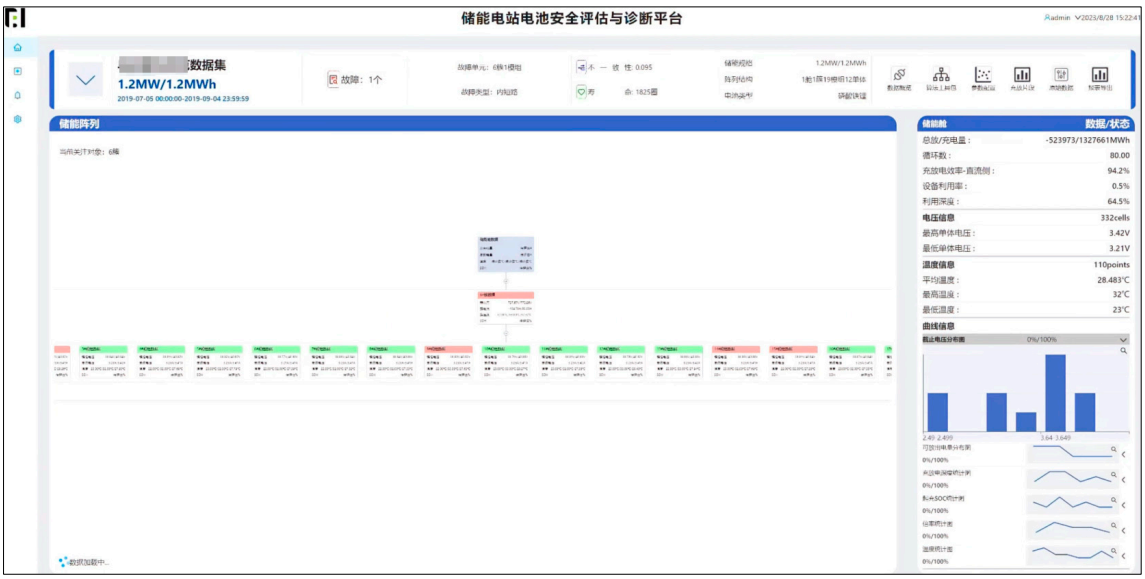

Figure 4. BFDS homepage.

3. Extraction and Prediction of Multi-Dimensional HFs

3.1. Aging Experiment

50Ah NCM622 square pouch batteries, with a rated capacity of 50 Ah, and upper and lower cut-off voltages of 2.75 V and 4.2 V respectively, manufactured by China Aviation Lithium Battery Technology Co., Ltd. (CALB) were selected for the experiment, as shown in Figure 5(a). The experimental instruments included the charge-discharge instrument manufactured by Neware, as shown in Figure 5(b) and the temperature and humidity test chamber manufactured by Doaho, as shown in Figure 5(c).

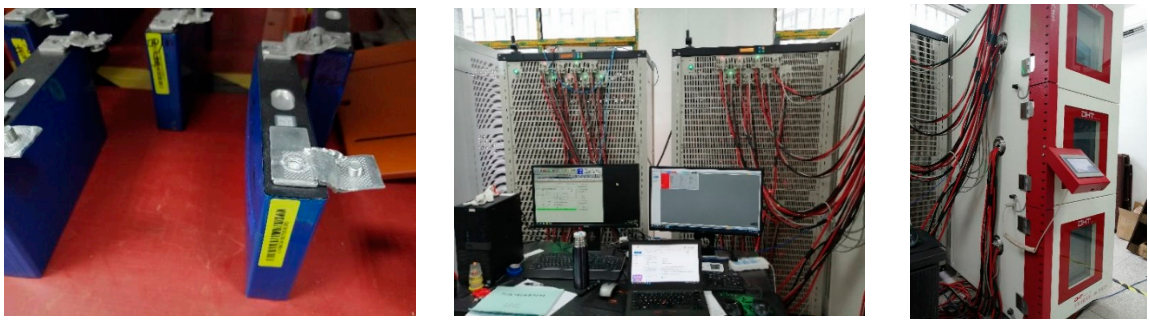

(a) **(b)** **(c)**

Figure 5. Experiment equipment: **(a)** NCM622 lithium-ion battery; **(b)** Neware charge-discharge instrument; **(c)** Doaho temperature and humidity test chamber.

Combined aging experiments were conducted using the chosen batteries at varying DOCs and C-rates, as shown in Table 2:

Table 2. Battery numbers for aging tests under different operating conditions.

DOD \ C	1	1.2	1.5	2

Preprints.org (www.preprints.org) | NOT PEER-REVIEWED | Posted: 22 March 2024 doi:10.20944/preprints202403.1129.v1

30	1,2	9,10	17,18	25,26
50	3,4	11,12	19,20	27,28
70	5,6	13,14	21,22	29,30
100	7,8	15,16	23,24	31,32

The batteries were charged and discharged based on the preset boundary conditions and were evaluated for their performance and capacity every calendar month. Taking the No. 8 battery as an example, partial cycles are shown in Figure 6:

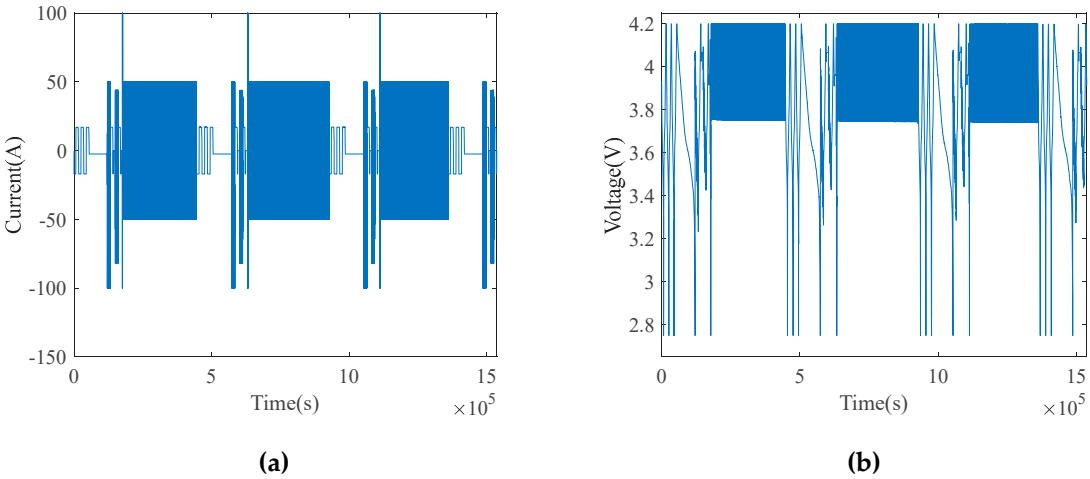

Figure 6. Partial experimental cycles of No. 8 battery: **(a)** current; **(b)** voltage.

The battery operation for one cycle is shown in Figure 7, where the areas a~e indicate the performance evaluation, including capacity, low-rate discharge, dynamic stress test (DST), Federal Urban Driving Schedule (FUDS), and hybrid pulse power characterization (HPPC) respectively, and f indicates the cyclic aging.

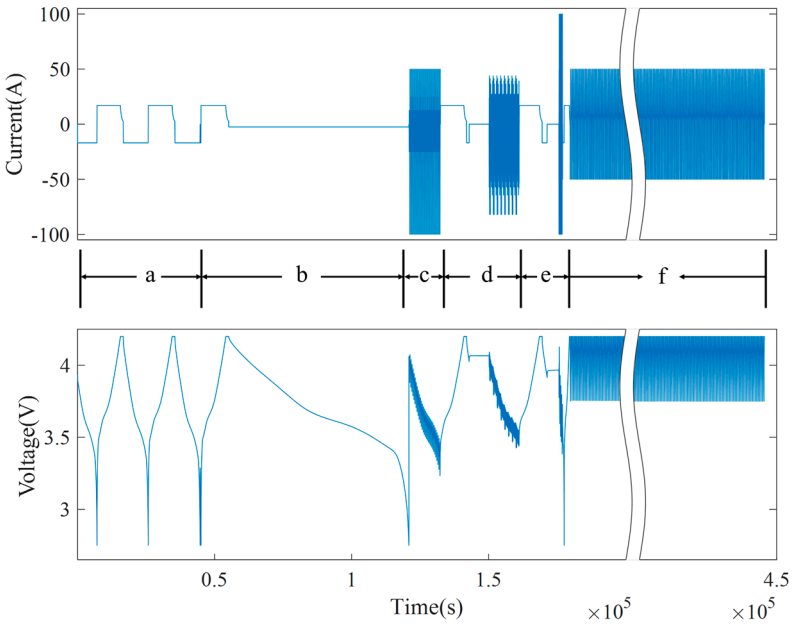

Figure 7. One experimental cycle of No. 8 battery.

The experimental procedure is described as follows:

 doi:10.20944/preprints202403.1129.v1

1. **Actual capacity test**: Discharge the batteries at a constant current of 1/3C to the lower cut-off voltage of 2.75 V. Charge them at a constant current of 1/3C to 4.2 V, and subsequently charge at a constant voltage until the current drops below C/20. Next, discharge them at a constant current of 1/3C to the lower cut-off voltage of 2.75V. Repeat this charge and discharge procedure two times. Refer to view a of Figure 8.
2. **Low-current discharge curve**: Charge the batteries at a current of 1/3C to the cut-off voltage, and discharge them at a current of C/20 to 2.75V after standing, as shown in view b of Figure 8.
3. **DST and FUDS conditions**: Set the batteries according to the *FreedomCAR test manual*[22], as shown in views c and d of Figure 8.
4. **HPPC**: Perform tests at varying SOC levels[23]. After the batteries are fully charged, gradually discharge them to 80%, 60%, 50%, 40% and 20% SOC for evaluations. Specifically, discharge them at a current of 2C for 18s, after setting them aside to stand for 40s, charge them at 1C for 10s, and then set them aside again to stand for 40s. Then charge the batteries with a current of 2C for 18s, after setting them aside to stand for 40s, discharge them at a current of 1C for 10s, and finally set them aside to stand for 40s. Refer to view e of Figure 8.

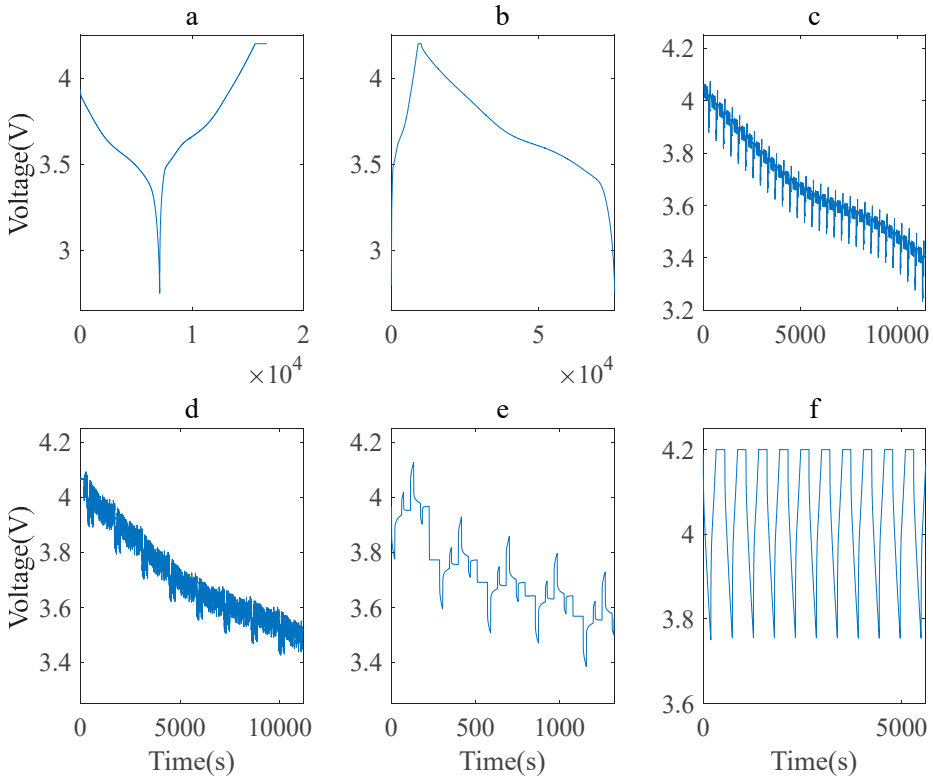

Figure 8. Items within a test cycle for No. 8 battery: **(a)** capacity; **(b)** low-rate discharge; **(c)** DST; **(d)** FUDS; **(e)** HPPC; **(f)** aging cycles.

The battery experiments are terminated when the battery capacity diminishes to 80% of the rated capacity, and the end of the battery life is recorded. Should any experimental battery exhibit significant bulging and leakage, the corresponding experiment should be halted promptly. The aging curves of all batteries are depicted in Figure 9, and those derived from polynomial fitting are illustrated in Figure 10.

 doi:10.20944/preprints202403.1129.v1

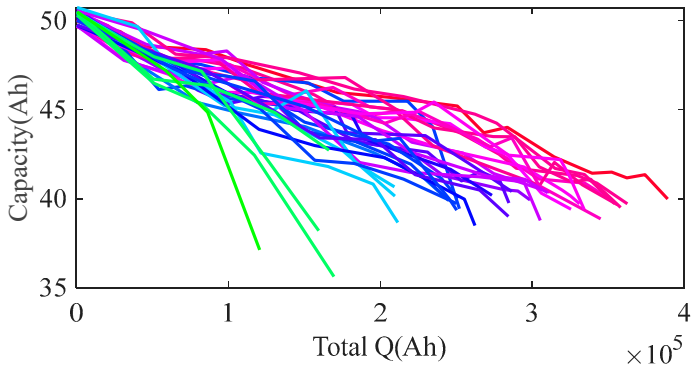

Figure 9. Aging curves of all batteries between capacity and cumulative throughput quantity (Total Q).

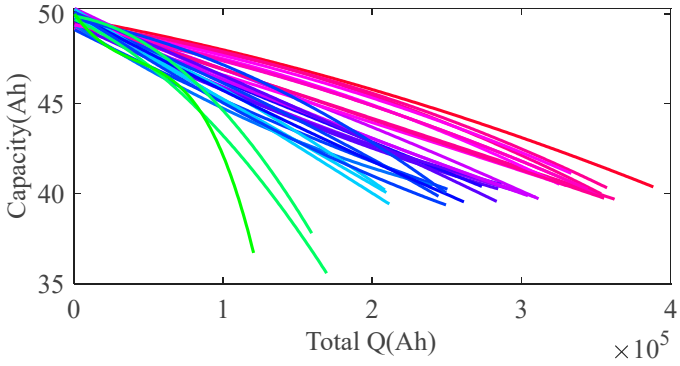

Figure 10. Aging curves of all batteries after polynomial fitting.

The cycle life of No. 3 battery was more than 40% shorter than that of No. 4 battery under the same conditions due to manufacturing defects. No. 30 battery experienced bulging and leakage at an SOH of 0.844, leading to the termination of the experiment. These two batteries were excluded from subsequent analysis.

3.2. Extraction of HFs

A health feature system for battery cells adaptable to various conditions has been developed from summarizing research findings over many years, as shown in Table 3.

Table 3. HF system.

Extraction method	HFs	Description
Measured data※[24] (applicable for cells, modules, and systems)	Self-discharge rate	To identify serious energy loss.
	Temperature rise rate	To identify temperature-related performance, such as serious self-heating and poor heat dissipation.
	Available charge/discharge capacity	To diagnose failures such as energy response absence, excessive attenuation rate, and capacity diving.
	Relaxation-related features, such as recovery time, and recovery slope	To diagnose reduced energy efficiency, insufficient power, etc. if failure to quickly return to normal after excitation.

 doi:10.20944/preprints202403.1129.v1

	Hysteresis voltage	To analyze whether the power performance degrades.
	Difference curves and associated features, such as ICA[25], DTV[26]	To analyze performance details as a function of Voltage, Temperature, or Pressure, such as power, energy, and heat production.
	Resistance, such as ohmic resistance, polarization resistance	To analyze energy performance degradation and power performance degradation.
	Coulombic efficiency[27]	
	Description of the change in the charging curve, such as capacity variance (VAR) ※[1,28]	
	A series of features based on the CCCV curve[29]	
Equivalent circuit model (applicable for cells and modules)	R[30], C[31] and CPE[32] of equivalent resistance	To evaluate attenuation by comparing with relevant values of normal batteries of the same specification
Experimental data	HPPC Resistance[33] (applicable for cells and clusters)	To analyze power performance degradation
	EIS parameters[34](applicable for cells)	To reflect the physicochemical properties of internal materials and detect underlying failures from the perspective of impedances.
Algorithm-based state estimation (applicable for cells, modules, and systems)	SOC※[35], SOH※[14], [25,36], SOE[37], SOP※[38], SOT※[39], etc.	To comprehensively analyze energy performance degradation and power performance degradation as a mature technique based on numerous studies.
Statistics on stacking relationship ※[1,19,29], (applicable for modules and systems)	Statistical analysis of extreme values and variances of voltage/temperature in modules	To screen abnormal cells or evaluate module consistency.
	Statistical analysis of extreme values and variances of inter-cluster current	Screen abnormal clusters or evaluate cabin consistency.
	Various types of measurable data or HFs may be used to statistically analyze battery systems at different layers. Specific examples are omitted in this paper.	
Electrochemical model※[40,41] (applicable for cells)	Physical and chemical parameters, such as maximum available lithium-ion concentration, SEI film resistance, overpotential, resistance of components, lithium-ion	To analyze energy and power attenuation and identify root causes based on electrochemical mechanisms[42].

 doi:10.20944/preprints202403.1129.v1

	concentration distribution, and particle sizes of active materials

The extraction methods of features marked with ※ are omitted in this paper, as they are detailed in the authors' previous articles. The mature extraction methods of other HFs in this research field are also omitted, as they can be found in publications of relevant research conducted by other scholars. It is important to note that calculating all features in the table is not necessary; selections should be made based on actual data quality, operating conditions, and computing power configuration. In Section 4, a comprehensive performance scoring method is introduced to support analysis using available HFs. Comparative evaluation can be achieved in parallel by ensuring the input of the same HFs and the same application scenario, without specifying the number and type of HFs.

Taking the No. 8 battery in the above experiment as an example, several features are described as follows:

1. **Capacity variance (VAR)**. As shown in Figure 11, the available discharge capacity at identical ΔV decreases with aging progression, resulting in steeper curves of differences from the initial test. Figure 12 shows a strong correlation between VAR and SOH.

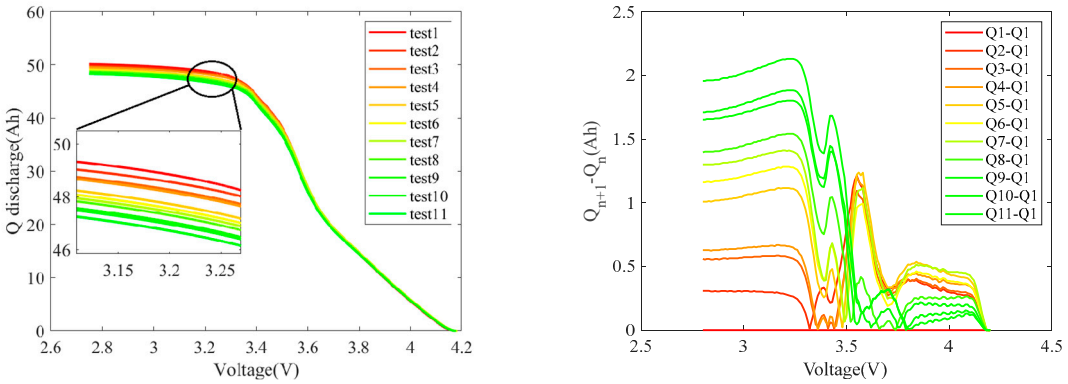

(a) **(b)**

Figure 11. Calculation process of VAR: **(a)** Original V-Q curve; **(b)** Discharge difference curve based on test 1.

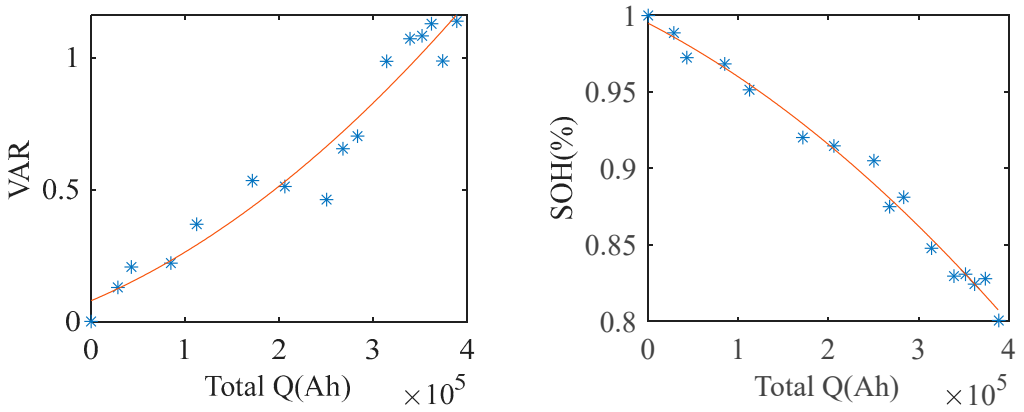

(a) **(b)**

Figure 12. Strong correlation between VAR and SOH: **(a)** scatter plot and fitting curve of VAR; **(b)** scatter plot and fitting curve of SOH.

Preprints.org (www.preprints.org) | NOT PEER-REVIEWED | Posted: 22 March 2024 doi:10.20944/preprints202403.1129.v1

2. **Resistance**. The ohmic and polarization internal resistances can be calculated through the HPPC test according to literature [43]. Refer to Figure 13 and Formula 8.

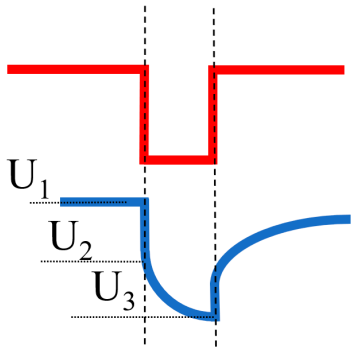

Figure 13. Partial enlarged view of HPPC test.

$$R_{Ohm} = (U_1 - U_2) / I$$
$$R_{Pol} = (U_2 - U_3) / I \quad (8)$$

Figure 14 displays the HPPC curves for multiple tests of No. 8 battery, illustrating that voltage changes intensify under the same current excitation with aging progression. Figure 15 shows the change curves of ohmic and polarization internal resistances.

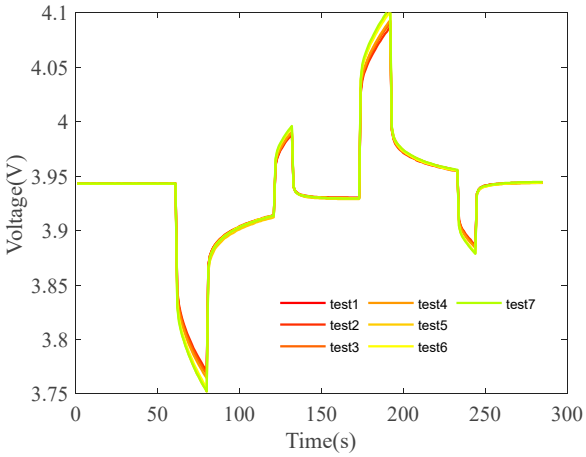

Figure 14. HPPC data from multiple tests.

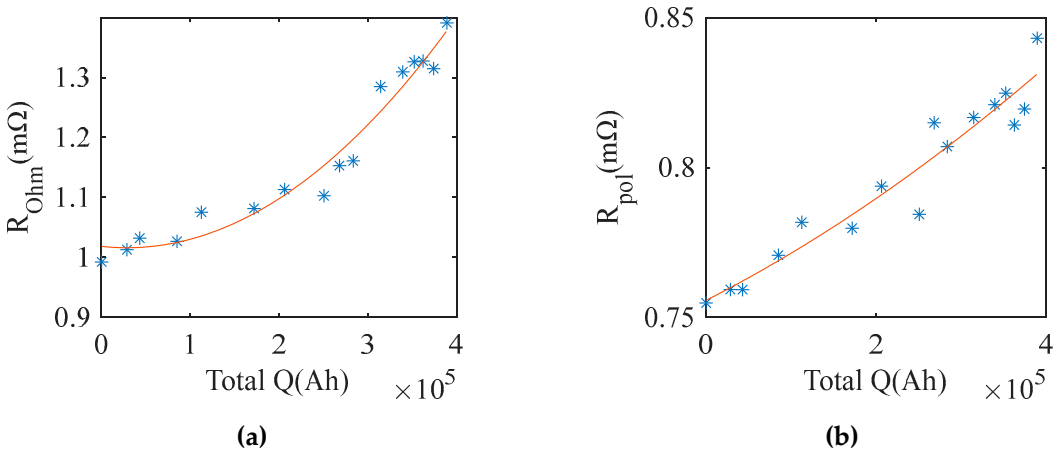

Figure 15. Resistance: (a) Ohmic resistance; (b) Polarization resistance.

 doi:10.20944/preprints202403.1129.v1

3. **Incremental capacity analysis (ICA)**. Figure 16(a) shows the original IC curve of a single test, subjected to smoothing. Figure 16(b) shows the IC curves of multiple tests, indicating decreasing peak values, rightward shifting peak positions, and narrowed peak areas with aging progression. Figure 17 shows the variation curves of peak values and peak areas, respectively.

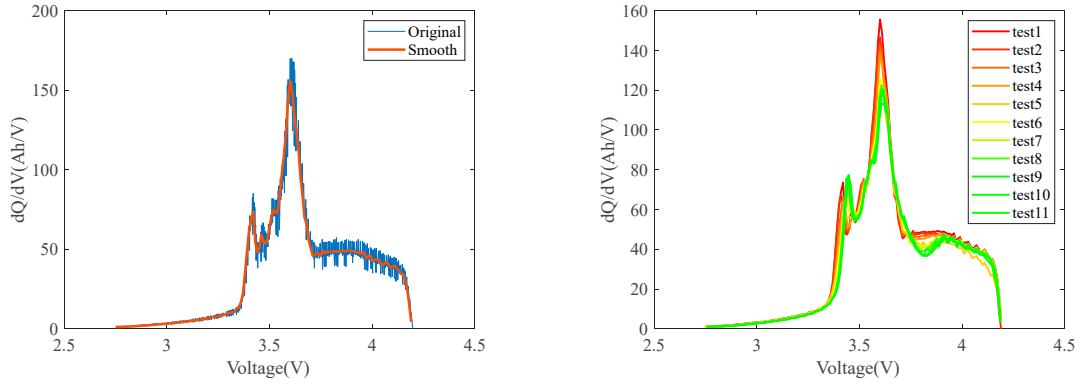

(a) **(b)**

Figure 16. IC curves: **(a)** Original IC curve and smoothed IC curve; **(b)** A set of IC curves from multiple tests.

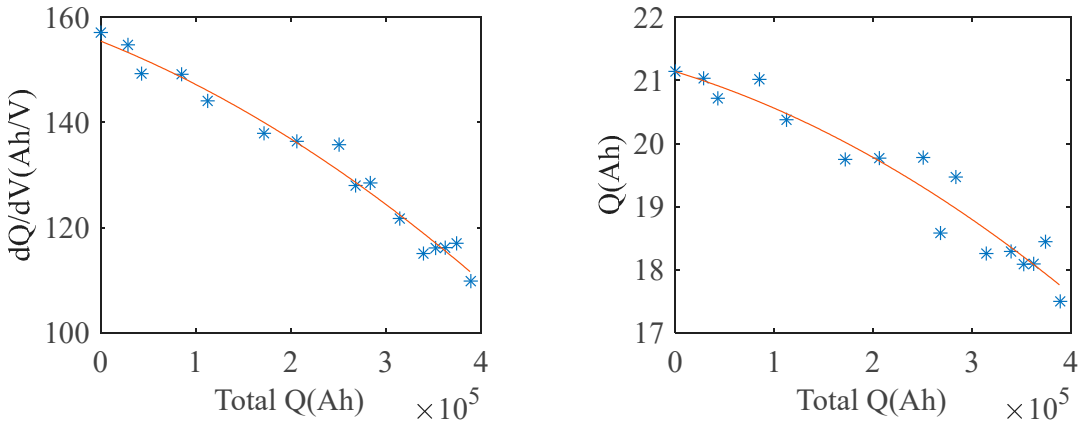

(a) **(b)**

Figure 17. IC features: (a) Peak value; (b) Peak area.

4. **Relaxation**. Relaxation refers to the process in which voltage slowly returns to a specific stationary stage upon the conclusion of excitation. The recovery to 3.91 V upon the conclusion of excitation was considered for current calculations. Figure 18 illustrates the recovery process following the removal of excitation during multiple HPPC tests. As shown, the recovery process is prolonged with aging progression. Figure 19 shows the variation curves of relaxation time and slope.

Preprints.org (www.preprints.org) | NOT PEER-REVIEWED | Posted: 22 March 2024 doi:10.20944/preprints202403.1129.v1

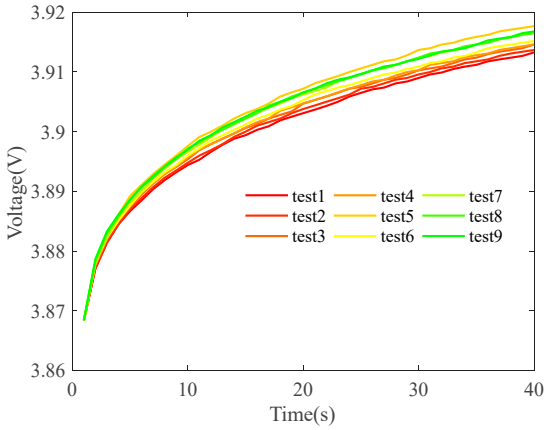

Figure 18. Enlarged view of relaxation during multiple tests.

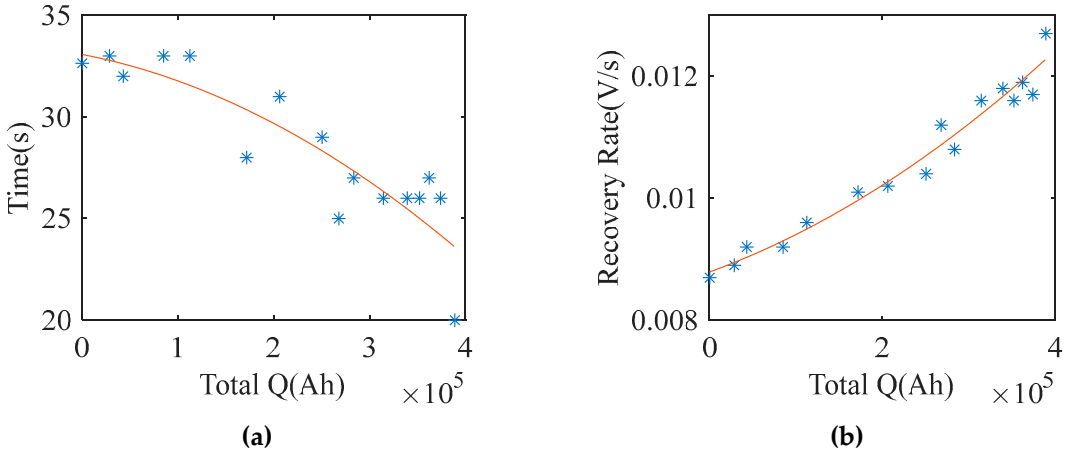

Figure 19. Relaxation features: (a) recovery time; (b) maximum recovery slope.

3.3. Prediction of HFs

A prediction method is proposed, which integrates modeling based on experimental data to generate the aging rates of HFs along their respective paths, and incorporates the projection of cumulative throughput quantity for predicting HF values in the end-of-period. The main idea is shown in Figure 20.

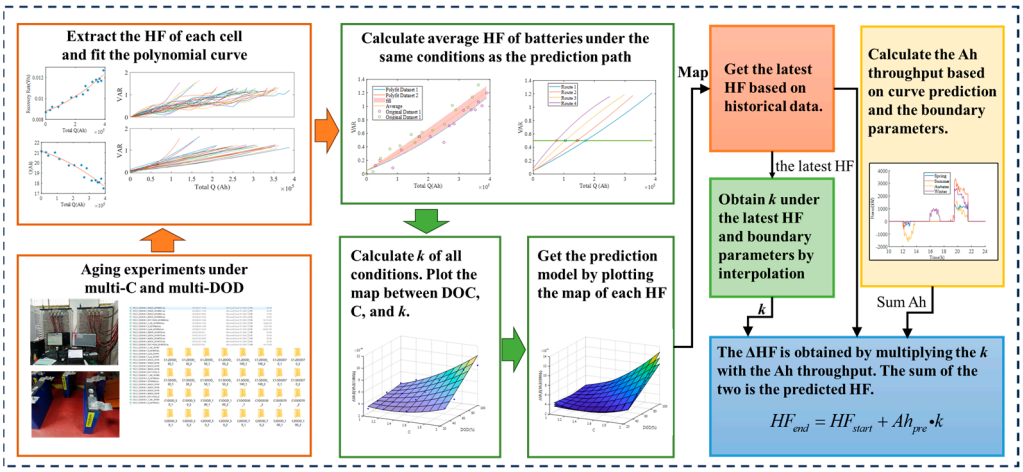

Figure 20. HF Prediction Procedure.

 doi:10.20944/preprints202403.1129.v1

Sets of mean HF curves under all conditions were plotted, as seen in Figure 21, with VAR taken as an example. The curves were then subjected to polynomial interpolation fitting.

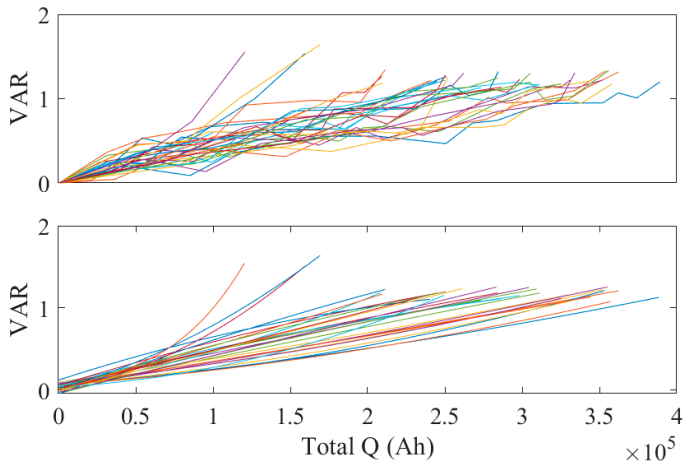

Figure 21. Original VAR curve set and fitted curve set of all batteries.

Two rounds of tests were carried out for identical conditions, and the calculated mean values of VAR represent the averages of a normal distribution, as shown in Figure 22.

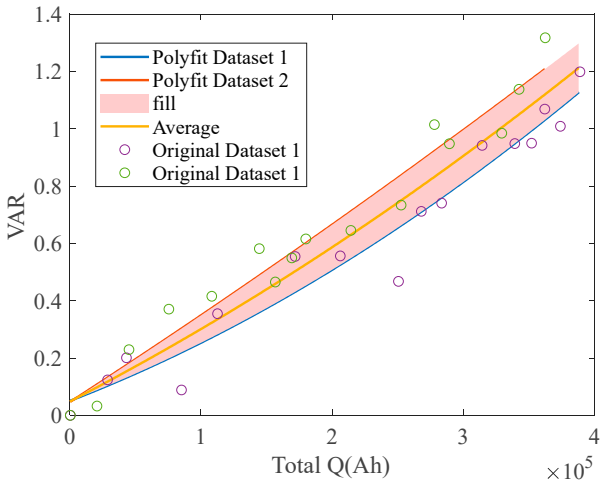

Figure 22. Statistical distribution of calculated VARs for two batteries.

Experimental curves representing the 95% confidence interval were used to simulate inconsistent changes during the simulation process, as illustrated in Section 5.2, rather than being incorporated here. For the abnormal No. 3 and 30 batteries, average values were derived from the data of normal cells from the same test, and rational confidence intervals were chosen for them based on two rounds of tests with similar conditions. For the convenience of illustration, several curves were taken for explanation, as shown in Figure 23. Subsequent aging paths vary depending on variations in DOD and C and in association with the current VAR. Calculations of slope changes in curves at a specific VAR value yielded 16 slopes as a function of DOD and C. Three-dimensional scatter plots were created and later integrated into Figure 24 using two-dimensional interpolation.

 doi:10.20944/preprints202403.1129.v1

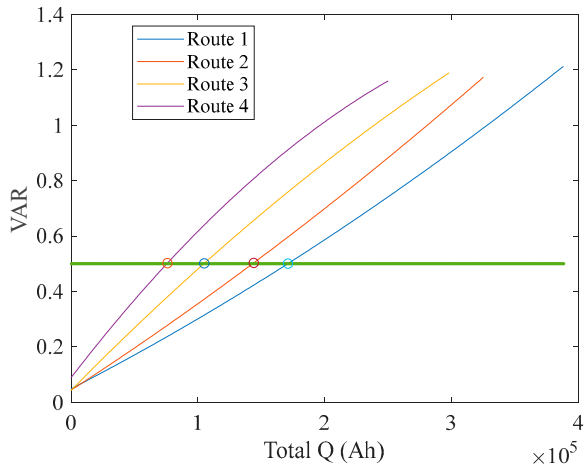

Figure 23. Schematic diagram of multiple paths with VAR = 0.5.

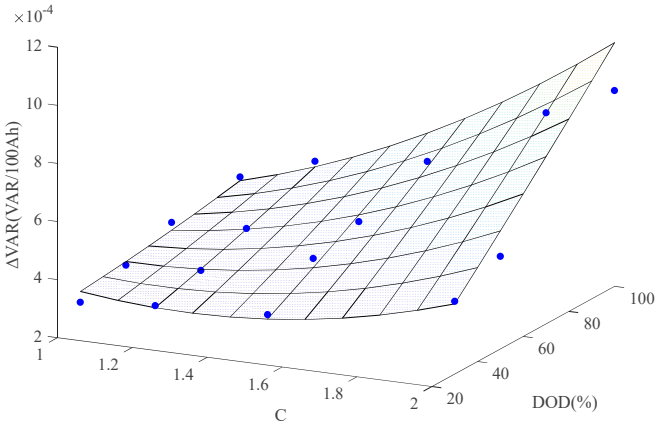

Figure 24. Map of C, DOD, and k with VAR=0.5.

It is evident that with larger C and DOD values, the change in the slope of VAR will increase accordingly. Change slopes beyond the scope of scatter points can be acquired through interpolation using the map.

As slope changes vary at different HFs, it is essential to account for the current actual HF value in calculations. Figure 25 displays the map with three VAR values. In this figure, as VAR increases, ΔVAR exhibits a greater increase under identical charge/discharge capacities.

 doi:10.20944/preprints202403.1129.v1

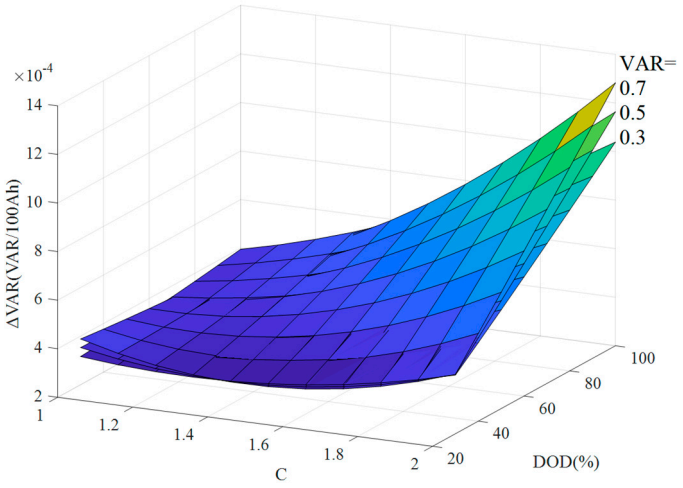

Figure 25. Map of C, DOD, and k with VAR=0.3, 0.5, and 0.7.

With actual HFs at the period outset, the variation rate (k) corresponding to DOD^{limit} and C^{limit} is derived through interpolation using the respective map. The alteration in Ah throughput is projected based on typical curves of the next period. Subsequently, the HFs following a period of operation are predicted using the formula below:

$$HF_{end} = HF_{start} + Ah_{pre} \bullet k \tag{9}$$

Where, HF_{end} denotes HF at the closure of the specific timeframe for prediction, HF_{start} denotes the current HF, and Ah_{pre} denotes the approximated total charge/discharge.

This calculation method is applicable for predicting results for operation at constant DOD and C values throughout the full lifetime, using the initial feature values as the starting point. Nevertheless, there are varying DOD and C values in actual operation, making it almost impossible to maintain consistent conditions. Hence, it is theoretically appropriate to modify the DOD and C values after a specific aging phase before conducting further experiments, and calculate slope changes using the experimental data acquired in the subsequent phase. However, conducting such experiments involves numerous combinations that may be impractical, not to mention the limited practical significance. The following two assumptions are proposed, which are adequate to underpin the solving process of the optimization model.

Hypothesis 1: The DOD and C values of the current operation predominantly influence the subsequent aging process, irrespective of the historical operating conditions' contribution to underlying failures. That is to say, attention should solely be focused on *k* values resulting from values of DOD and C for subsequent phases.

Hypothesis 2: All daily conditions in the next period are regarded as the most severe, and all batteries function based on the maximum boundaries established through optimization. The predicted results for operation under such circumstances serve as a reference for the optimization model.

In a majority of cases, the most severe conditions rarely occur in actual control. Consequently, the actual aging status tends to be worse compared with the predicted values. Nonetheless, multiple batteries at the same layer generate identical operating curves, and performance differences emerge irrespective of whether they function at extremes. Additionally, this simplified method significantly enhances calculation efficiency.

Figure 26 shows exemplary maps for several HFs:

 doi:10.20944/preprints202403.1129.v1

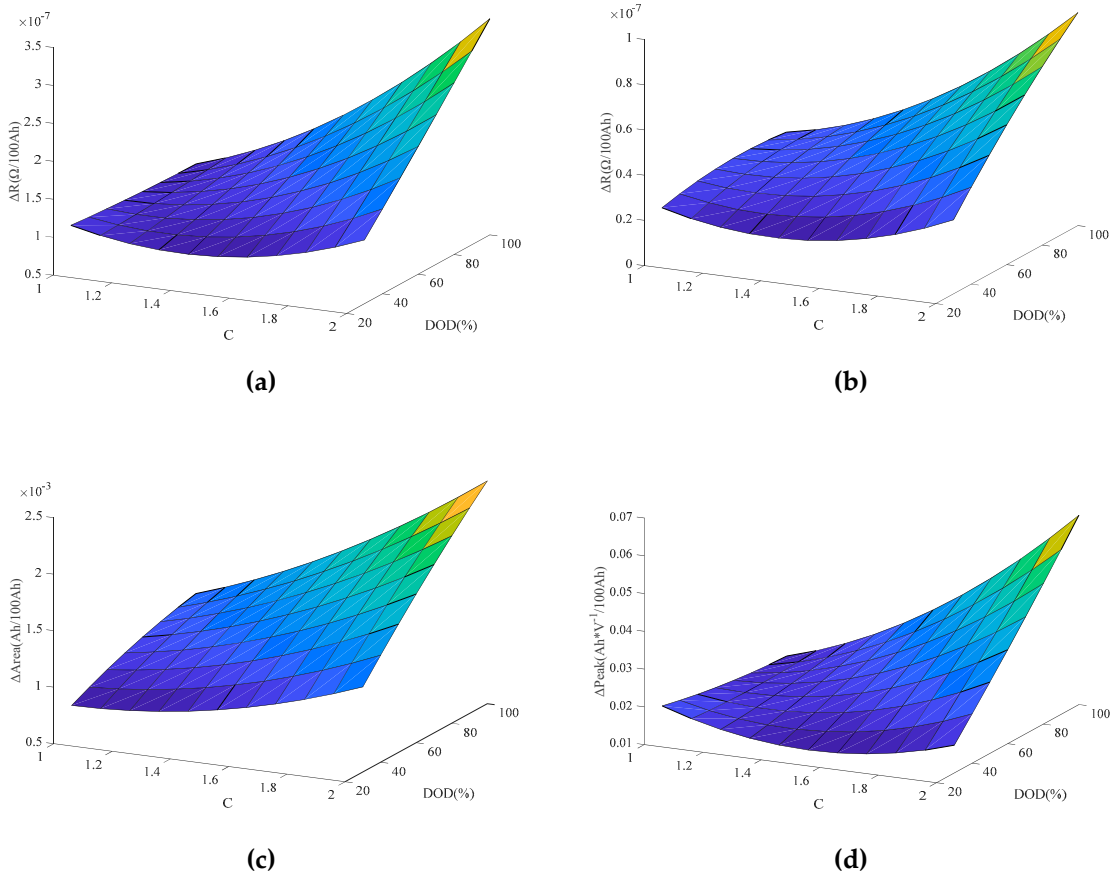

Figure 26. Map of **(a)** Ro, **(b)** Rp, **(c)** IC Area, and **(d)** IC Peak.

4. Prediction Method of Aging Cost for Energy Storage System

In traditional energy application scenarios, regular charge and discharge processes with constant currents were prevalent, where battery charge/discharge capacities were considered as the primary performance indicator. As a result, conventional methods for determining battery residual value often involve calculating capacity SOH. SOH represents the lifetime value including cascade utilization subsequent to decommissioning[44]. However, as applications expand to encompass more intricate scenarios, integrating multiple performance indicators crucial for energy and power applications becomes imperative. Evaluating battery functionality can no longer rely solely on capacity SOH. Two batteries with identical SOH may exhibit varying performances despite following the same operating curve. From this standpoint, the authors established a comprehensive performance scoring system based on multi-dimensional HFs. The calculation methods have been detailed in our prior research[1]. This system primarily seeks to reveal distinctions in overall operational performance among batteries at the same layer.

In that study, an unsupervised learning-based multi-appraiser model is proposed, incorporating multiple clustering algorithms for categorization into "good" and "bad", subsequently converting these classification outcomes into scores via statistical methods. Figure 27 illustrates a comparison of comprehensive performance scores utilizing data from the initial 100 cycles and accumulations (Numbers of cells have been reordered based on score, which is different from the experimental numbers in Table 2), showcasing an obvious correlation between them, particularly for batteries that were prematurely terminated from the experiments.

 doi:10.20944/preprints202403.1129.v1

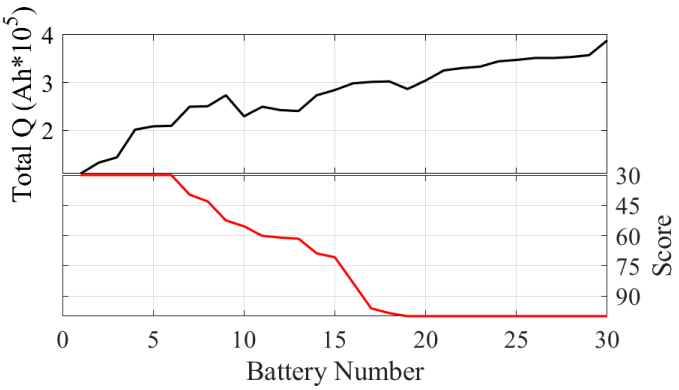

Figure 27. Correlation between Score and Total Q.

This method not only effectively sidesteps the possible challenges associated with excluding features in calculations but also eradicates the necessity for feature selection. The exclusion of features in calculations due to conditions or data quality is consistent across all batteries.

After multiple batteries have been operating under the same operating conditions for a period of time, the degradation cost of each battery is different. This varied degradation can be effectively quantified using the comprehensive performance scoring system. Lower scores indicate higher aging costs due to inferior performance compared to other batteries in one or more aspects. Without optimization in the control strategies, battery performance is prone to continuous degradation, resulting in a continuous decline in actual commercial value within current operating scenarios. In summary, SOH reflects the objective depreciation of batteries over time and the scoring system incorporates variances from other batteries under current operating scenarios. The strategy proposed in this paper still utilizes SOH as the main criterion for residual value calculation, subjected to weighting using comprehensive scoring. The resulting calculation formula for residual values $Value_{residual}$ is expressed as follows:

$$Value_{residual} = (Value_{initial} - Value_{recycling}) \cdot \frac{SOH - SOH_{retired}}{100 - SOH_{retired}} \cdot Score \tag{10}$$

Where, $Value_{initial}$ denotes the initial value, $Value_{recycling}$ denotes the recovery value, and $SOH_{retired}$ denotes the SOH recommended for decommissioning. The initial cost is calculated by spreading out the total cost of integrated modules across individual cells through amortization.

Taking into account the potential recovery of battery capacity, which can lead to increasing scores due to optimization within the operational domain, it is possible to generate higher residual values compared to the preceding operational period. The consequent negative aging costs may introduce anomalies in the solving process aimed at minimizing aging costs through optimization. A zero aging cost suggests that the battery's operating boundaries have been rationally optimized. The formula for calculating aging costs is expressed as follows:

$$Cost^{p}_{aging} = \max(Value^{p-1}_{residual} - Value^{p}_{residual}, 0) \tag{11}$$

Where, $Value^{p-1}_{residual}$ denotes the equipment residual value at the end of the preceding period (or at the beginning of the current period), which is obtained by calculating the latest HFs using actual operational data. $Value^{p}_{residual}$ denotes the equipment residual value at the end of the current period. According to Section 3.3, Ah_{pre} is approximated in accordance with boundary parameters, and k is deduced accordingly, resulting in the prediction of $Value^{p}_{residual}$. For example, the aging cost curve of the No. 1 experimental battery is not linearly related to SOH variations in the prediction based on SOH and scoring as shown in Figure 28.

Preprints.org (www.preprints.org) | NOT PEER-REVIEWED | Posted: 22 March 2024 doi:10.20944/preprints202403.1129.v1

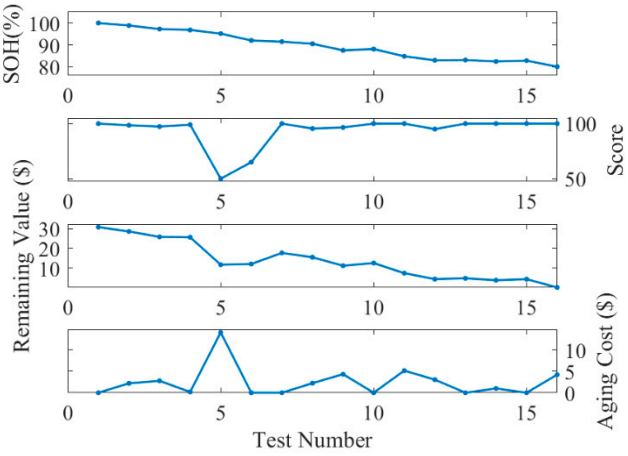

Figure 28. Case of aging cost based on SOH and score.

The aging costs of battery clusters can be predicted by accumulation according to their topological relationships. If inconsistencies escalate among cells within a cluster, the count of cells with low scores rises, leading to elevated aging costs for the cluster. Consequently, fewer power is assigned to the cluster to impede the advancement of these inconsistencies.

5. Case Study

5.1. Description of Application Scenario

At a "Source-Grid-Load-Storage park" including PV, industrial load and citizen load, factories within the park are supplied by a 10 kV medium-voltage line with a rated capacity of 10MW via a dedicated transformer, as shown in Figure 29. Additionally, the surrounding residential areas are supplied also by this line via a public transformer. Data concerning industrial loads in this park were gathered and used to plot seasonal production load curves as shown in Figure 30. The annual PV output of the geographical region is shown in Figure 31, and the typical output curves fitted for four seasons are shown in Figure 32.

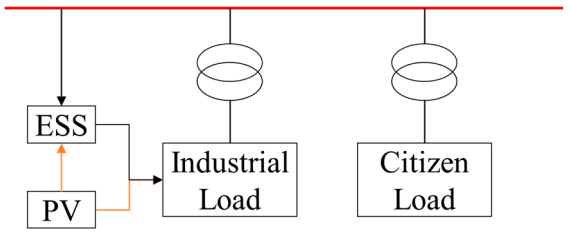

Figure 29. Schematic diagram of power supply and consumption structure in the park.

 doi:10.20944/preprints202403.1129.v1

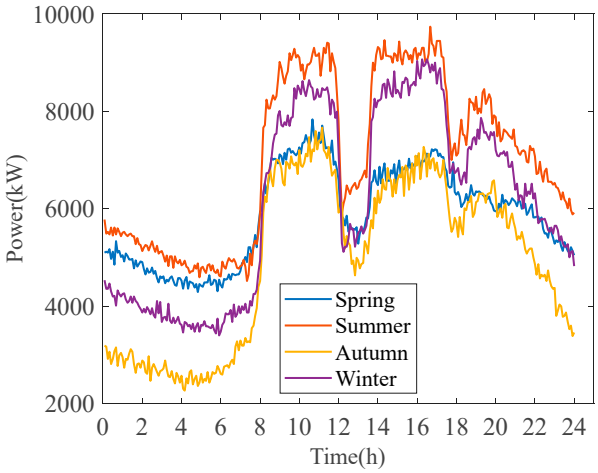

Figure 30. Typical curves of industrial loads in four seasons.

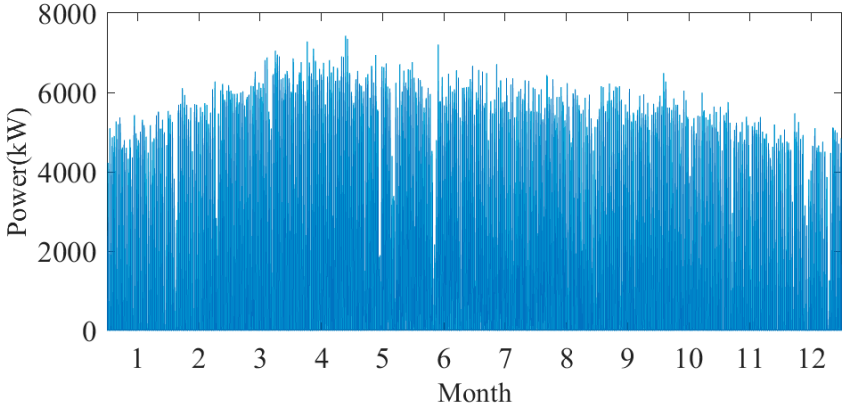

Figure 31. Annual PV output.

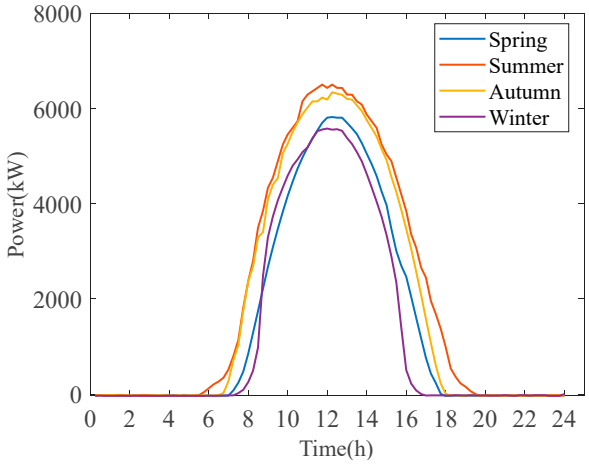

Figure 32. Typical curves of PV output in four seasons.

The energy storage station follows the following operational rules: PV power is to be primarily consumed locally, with surplus power stored in cases where immediate consumption is not feasible. To prevent overloading of the dedicated transformer within the park, any surplus loads should be served from the energy storage system. In addition, to prioritize ensuring power supply to residential

 doi:10.20944/preprints202403.1129.v1

loads during nighttime hours, the local power grid company enforces a time-of-day tariff system aimed at incentivizing the reduction of nighttime loads within the park. Consequently, every day from 19:30 to 21:30, the energy storage system discharges to maintain loads below 5,000 kW for the dedicated transformer serving industrial loads. Figure 33 showcases the process of deriving energy storage operation curves during the summer months: PV power is first consumed by loads, and any excess is absorbed by the energy storage system, referred to as "ESS Charge". The curve labeled "Load from Grid" represents loads obtained directly from the grid without involving the energy storage system. The curve labeled "ESS Discharge Part 1" illustrates the energy storage system's supply to prevent line overloading, while "ESS Discharge Part 2" denotes the capacity reserved for residential nighttime consumption.

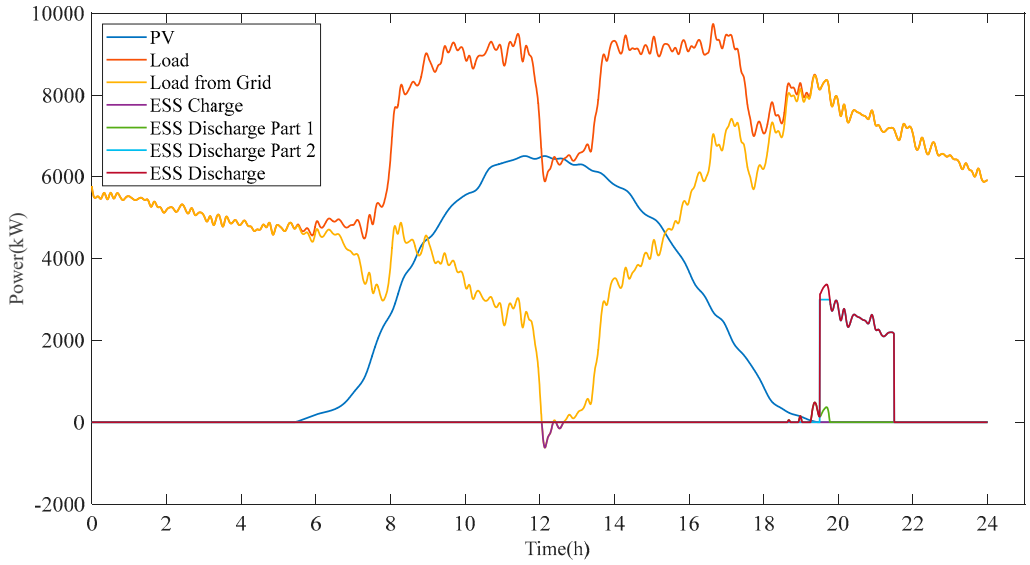

Figure 33. Schematic diagram of energy storage output in summer.

Similarly, the typical output curves in four seasons are plotted as shown in Figure 34:

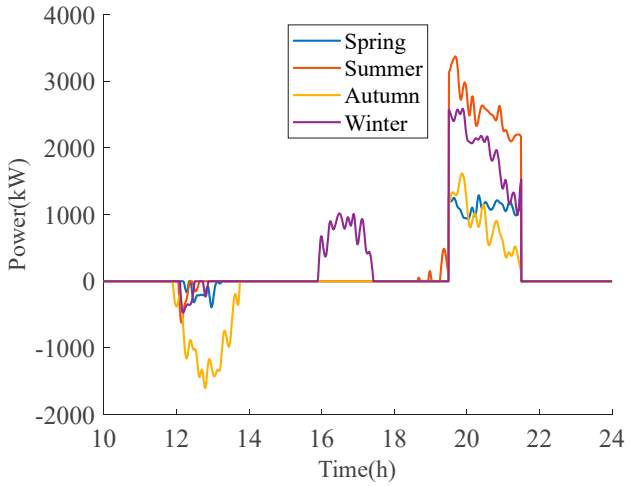

Figure 34. Typical curves of energy storage output in four seasons.

The resulting energy imbalance can be compensated by adjusting the nighttime charging power. Considering the plentiful wind power resources in the region, the energy storage station leverages lower nighttime tariffs to charge to the desired SOC. To simplify the processing, it was assumed that all energy storage units could be charged at a reduced rate during nighttime, which is omitted in subsequent steps for the convenience of plotting.

 doi:10.20944/preprints202403.1129.v1

5.2. Simulation Model of Energy Storage System

The energy storage system consists of a total of 20 cabins, and dispatching instructions are first evenly distributed among them, as shown in Figure 34. Each cabin is comprised of 12 clusters, with each under independent control by PCS. As the energy storage station was in the initial stage of trial operation, it has not been verified for prolonged operational durations. Therefore, Simulink was used to simulate a battery cabin for algorithm verification. The simplified electrochemical model, as outlined in our prior article[41], underwent parameter identification through experimental data before being incorporated into Simulink for operational simulation. The overall simulation model is shown in Figure 35.

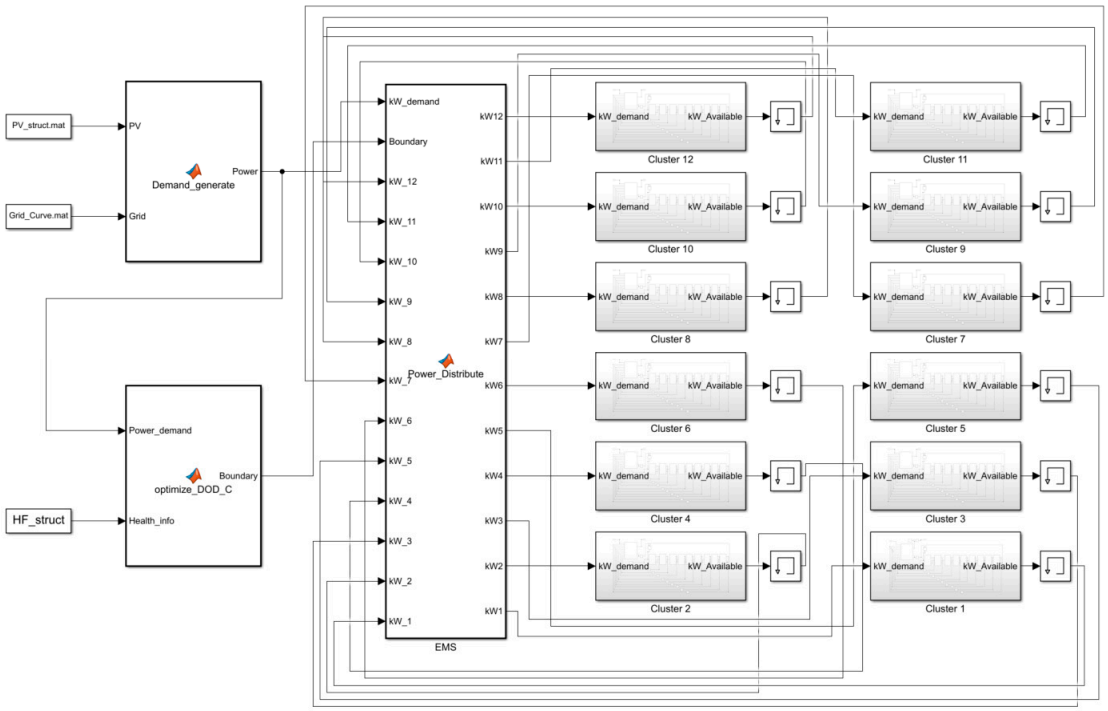

Figure 35. Overall Simulink model.

It was challenging to simulate each cell individually, especially considering the extensive computing power required. Each cluster within the energy storage system contained 162 cells distributed among 9 modules, with each module being treated as a simulation unit, assuming cells within a module are identical, as illustrated in Figure 36. Distinct initial SOH values were assigned to these battery modules, the SOH of a cluster was determined by selecting the lowest SOH among the modules within the cluster following the "buckets effect"[45].

 doi:10.20944/preprints202403.1129.v1

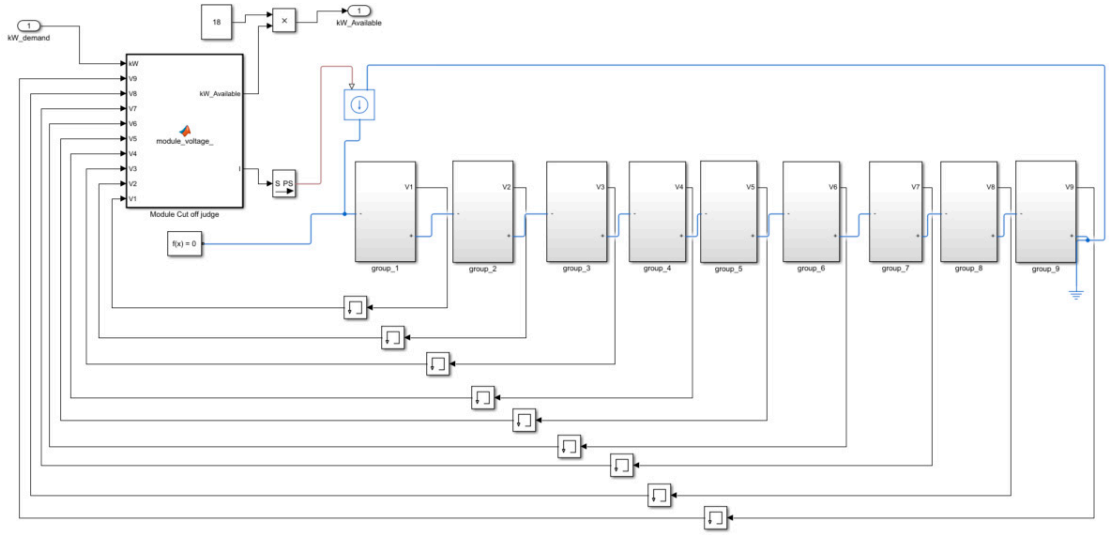

Figure 36. Simulation model within a cluster.

For aging evaluation, variations of HFs were calculated using the average DOD and C values during real operation. To simulate inconsistencies linked to manufacturing level, system integration, ambient temperature distribution within battery cabins, etc. under actual operating environments, the simulated HFs were randomly updated according to a normal distribution. As shown in Figure 37(a), with point A assumed to represent the calculated mean HF, and points B and C to delineate the upper and lower boundaries of the 95% confidence interval, random updates were confined within the shaded area shown in Figure 37(b).

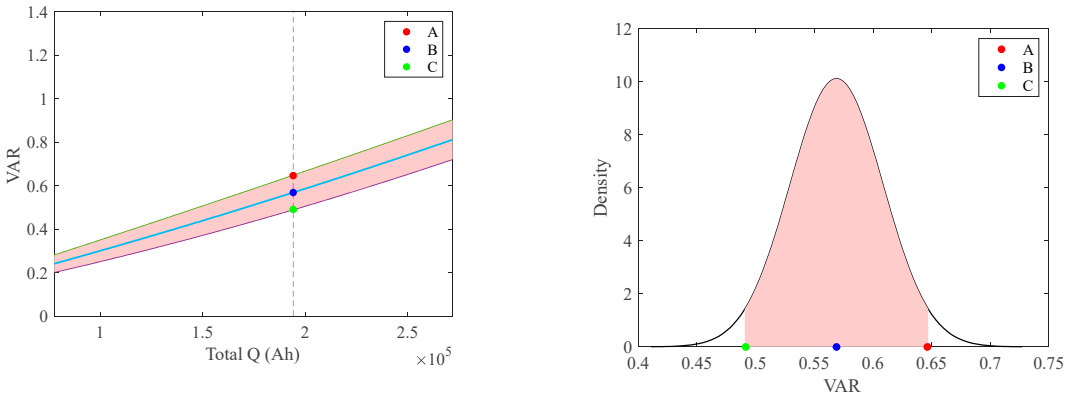

(a) **(b)**

Figure 37. Schematic Diagram of HF calculation based on normal distribution: **(a)** Average value and calculated value according to total Q; **(b)** Probability density distribution.

It's important to note that HFs can be calculated synchronously with real data without introducing artificial inconsistencies in engineering applications.

5.3. Comparative Analysis of Results

For comparative analysis, simulations were conducted for the battery cabin utilizing two strategies, which are respectively the traditional equalized dispatching strategy and the differentiated dispatching strategy proposed in this paper. The simulations incorporated the following conditions: Any battery clusters with an SOH lower than 80% are suspended from responding to dispatching

 doi:10.20944/preprints202403.1129.v1

instructions. The unit cost of the battery system is assumed at 0.3667$/Wh and $Value_{recycling}$ is 0 after retirement. η is 95%.

Under the differentiated dispatching strategy proposed in this paper, the operation profile under typical conditions in summer is shown in Figure 38.

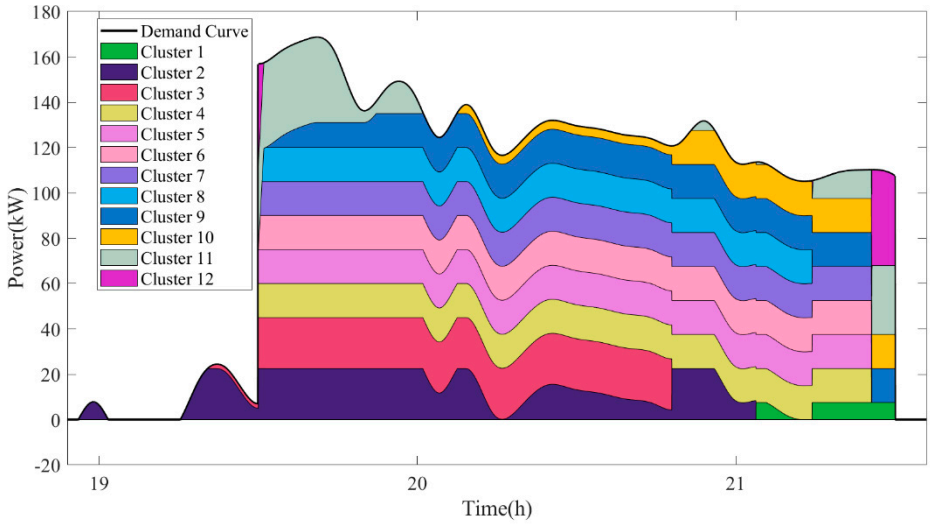

Figure 38. Stack graph of typical output in summer under differentiated dispatching strategy.

Under the equalized distribution strategy, the operational profile at evenly distributed power levels is shown in Figure 39:

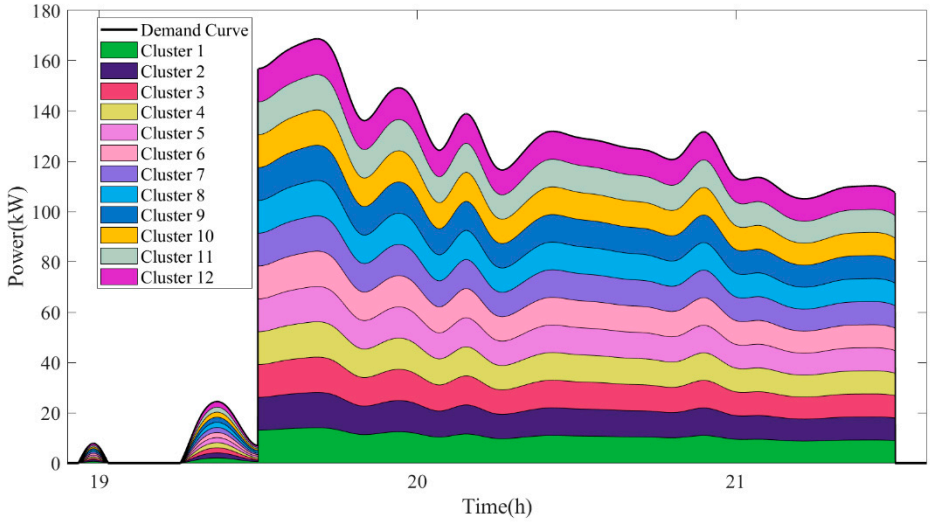

Figure 39. Stack graph of typical output in summer under equalized dispatching strategy.

To avoid unexpected results stemming from operating procedures with random inconsistencies, three rounds of operation simulations were conducted alongside solving for optimization, using the same SOH initialization values of 0.94, 0.982, 0.981, 0.986, 0.983, 0.974, 0.973, 0.975, 0.977, 0.972, 0.997, and 0.998 for respective clusters. The following typical integration defects were considered in initialization: abnormal cells in cluster 1, slight aging in clusters 2 to 5, consistencies in clusters 6 to 10 along with slight aging, and clusters 11 and 12 in good status. The 9 groups of cells in each cluster are randomly distributed according to the above assumptions. The initial SOH values of the aforementioned clusters were obtained by using the “bucket effect”.

The comparison of results is presented in Table 4:

 doi:10.20944/preprints202403.1129.v1

Table 4. Comparison of results from three rounds of simulation calculations.

	Round 1		Round 2		Round 3	
	Proposed method	Equalized method	Proposed method	Equalized method	Proposed method	Equalized method
Service life (quarterly)	58	50	54	49	60	51
Average aging cost per kilowatt-hour ($/kWh)	0.0759	0.0819	0.0785	0.0824	0.0749	0.812
Inconsistency (expressed as the sum of variances)	2.1821e-04	2.8150e-04	2.2413e-04	2.7615e-04	2.0047e-04	2.6590e-04

The first round of the solving process is meticulously outlined. Figure 40 presents a comparison of aging curves among the 12 clusters under the proposed method. These clusters using the proposed method halt in responding in summer with peak demands, after a nine-and-a-half-year operational duration, due to serious aging, as shown in Figure 41. With DOD and C constraints removed in summer, the clusters continue to operate with equalized distribution, yielding identical operating curves as shown in Figure 39. Furthermore, the differentiated dispatching strategy is sustained in other seasons, as exemplified in the winter operation shown in Figure 42. In the first quarter of the 14th year, cluster 1 is decommissioned but the remaining 11 clusters remain available in responding to instructions. In the next quarter, with the decommissioning of cluster 6, the battery cabin becomes incapable of responding to dispatching instructions, signaling its end-of-life stage.

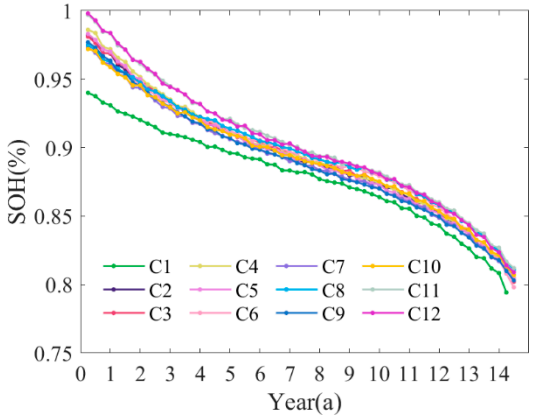

Figure 40. SOH variations under differentiated dispatching strategy.

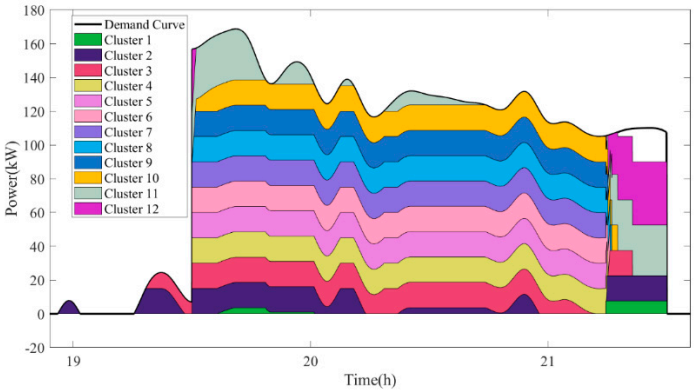

Figure 41. Stack graph of output insufficiency in summer under differentiated dispatching strategy.

 doi:10.20944/preprints202403.1129.v1

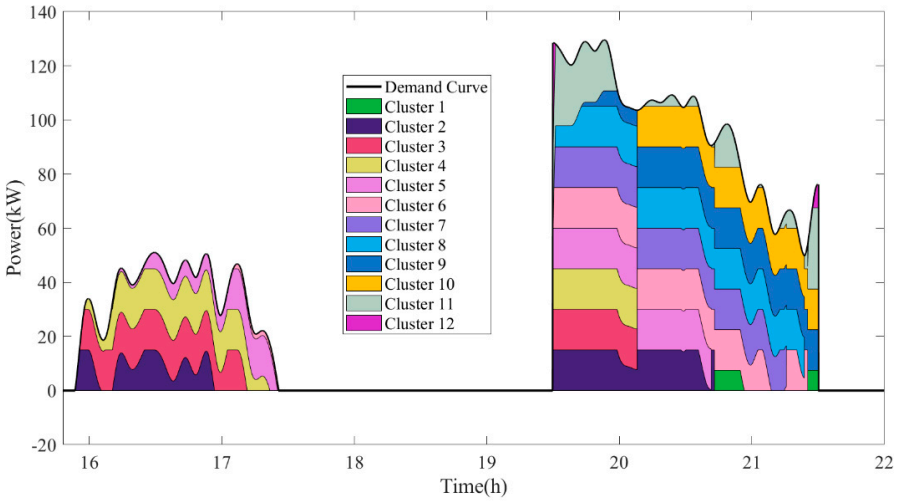

Figure 42. Stack graph of output in winter under differentiated dispatching strategy.

In this example, cluster 12 is initially defined as E and cluster 11 as D. There is an exchange between clusters 12 and 11 in their rotation status in the third quarter of the 4th year, and another exchange occurs in the first quarter of the 8th year. The rest of the clusters retain their status as S throughout the operational timeframe, exhibiting reductions in C^{limit} and elevations in DOD^{limit}. Figure 43 shows the boundary comparison between the initial state (Parameters 1) and transition threshold towards the equalized dispatching (Parameters 2):

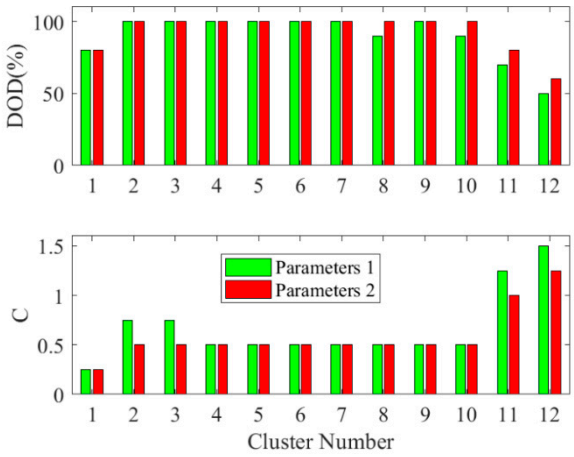

Figure 43. Comparison of boundary parameters.

Figure 44 shows the aging curves of the 12 clusters under the equalized method. When a cluster with inferior performance is disconnected upon reaching the cut-off voltage, power is redistributed equally among the others. Cluster 1 is decommissioned after the first quarter of the 12th year, followed by cluster 10 in the next quarter. Although the other batteries remain in good health, the cabin can no longer respond to instructions, as shown in Figure 45.

 doi:10.20944/preprints202403.1129.v1

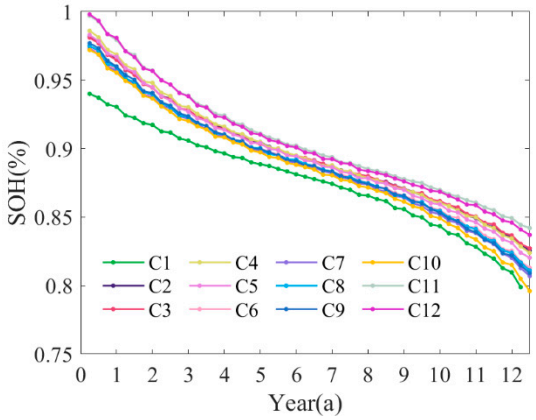

Figure 44. SOH variations under equalized dispatching strategy.

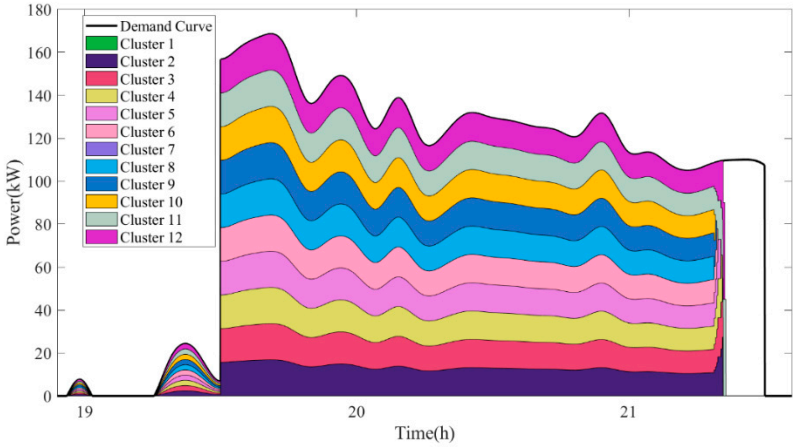

Figure 45. Stack graph of output before decommissioning under equalized dispatching strategy.

Under the differentiated strategy, aging exhibited a slower rate and tended to converge, whereas the equalized strategy led to contrasting trends. The former resulted in a 16% extension in service duration. Variances in SOH across clusters were calculated as an inconsistency indicator, and Figure 46 shows a comparison of cluster SOHs after decommissioning. The sums of variances were 2.1821e-04 and 2.8150e-04, respectively, amounting to a 22.48% decline.

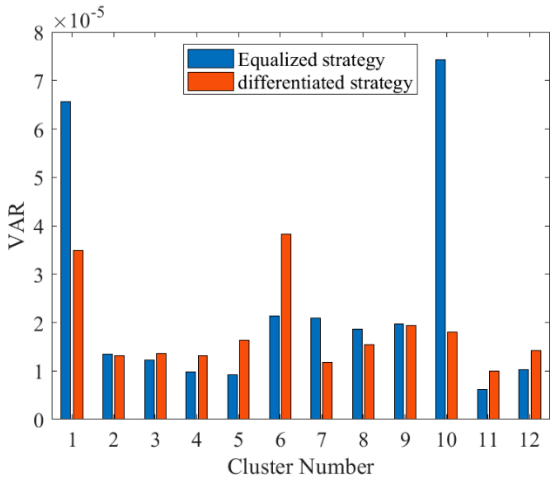

Figure 46. Comparison of SOH variances after decommissioning under two strategies.

 doi:10.20944/preprints202403.1129.v1

The aging costs per kilowatt-hour of clusters resulting from the proposed method is shown in Figure 47, and those from the equalized method are shown in Figure 48. Significant differences emerge among clusters in the initial phases under the proposed method. The aging progression of lower-quality batteries is decelerated by leveraging the presence of high-quality batteries, leading to a convergence in aging costs during the later stages. The total aging costs per kilowatt-hour is 0.0759 $ and 0.0819 $ respectively, with a reduction of 7.33%.

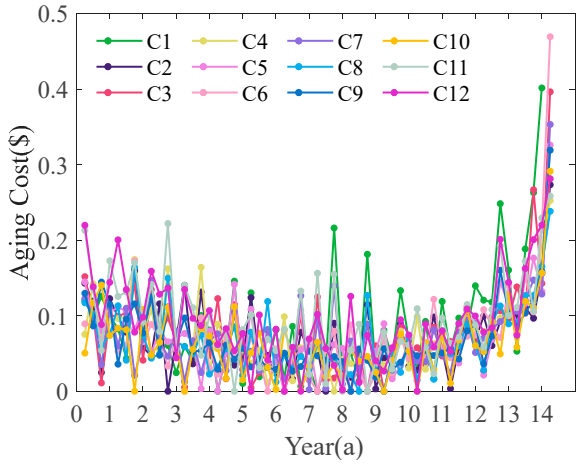

Figure 47. Annual aging cost per kilowatt-hour under differentiated dispatching strategy.

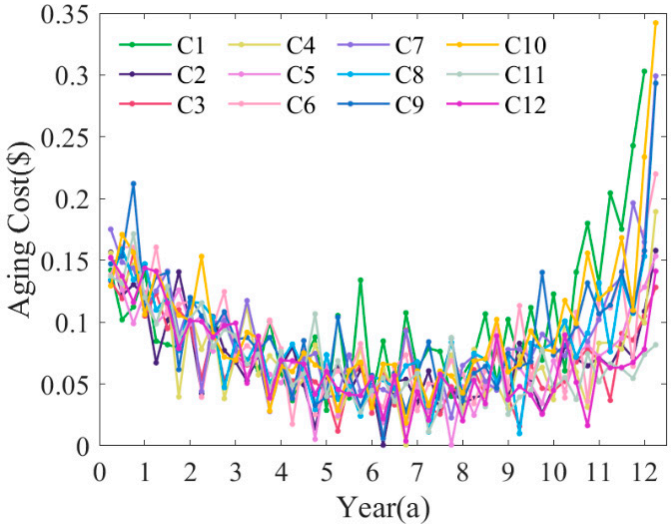

Figure 48. Annual aging cost per kilowatt-hour under equalized dispatching strategy.

In summary, the three rounds of simulation verification illustrated in Table 4 demonstrated an average extension of service life by 14.62%, a decrease in aging costs by 6.61%, and a reduction in inconsistencies by 21.98%.

6. Conclusions

To tackle the challenges posed by composite energy storage applications with escalating complexities in operating conditions, this paper presents a novel control strategy integrating an objective function to minimize aging costs, supplemented by the corresponding application procedure. With a focus on enhancing consistency and extending service life, this research accomplished the following tasks:

1. The optimization control strategy presented, along with its solving process, helps in reducing aging costs and extending the service life of energy storage systems. Furthermore, it improves module consistency, offering advantages for cascade utilization following module recombination.
2. The periodic rolling optimization mode proposed for integrating this strategy into engineering operation benefits not only from reducing the computational power needed for each optimization control but also from enabling iterative adjustments based on the actual operational status.
3. The aging cost evaluation introduced incorporates multi-dimensional features, rather than solely considering capacity SOH.

This study was conducted through experiments and simulations, and the findings were verified to some extent. It is still essential to conduct further research and application exploration from the following aspects in the future:

1. Due to time and equipment limitations, the comparative experiments were not sufficient. Variable intervals may be refined in the future, to establish a more accurate aging prediction model. Additionally, data collected during long-term operation revealed that batteries with high SOC and low operating frequency exhibited noticeable storage aging. In the subsequent strategy optimization, it may be beneficial to optimize SOC points after charging instead of performing a full charge each time.
2. Utilizing the universality of the proposed approach, models can be developed with a small amount of experimental data in scenarios involving other types of batteries. These models can then be used for simulations of aging under multiple variables to provide a reference. This approach can help in reducing the cost associated with long-term aging experiments.
3. Shortening the time span of each period allows for more refined optimization control in engineering applications.

Author Contributions: Conceptualization, X.W. and J.J.; methodology, J.J., L.W., J.C. and Z.W.; software, J.J. and J.C.; validation, W.Z., X.W. and Z.W.; formal analysis, L.W. and L.B.; investigation, X.W., J.J., L.B. and W.Z.; resources, W.Z., X.W. and L.W.; writing—original draft preparation, J.J. and X.W.; writing—review and editing, X.W., Z.W. and L.W.; visualization, J.C., J.J. and L.B.; supervision, X.W. and W.Z.; funding acquisition, W.Z and X.W. All authors have read and agreed to the published version of the manuscript.

Funding: This research was funded by National Key R&D Program of China, grant number 2021YFB2400700.

Data Availability Statement: The data presented in this study are available on request from the corresponding author.

Acknowledgments: Thanks to many masters, doctors and teachers from Chongqing University who have participated in the experiment for more than three years. Thanks to the trial operation scenario provided by the Three Gorges Source-Grid-Load-Storage Demonstration Base in Ulanqab, Inner Mongolia. Thanks to the scholars mentioned in the references for their research results on health feature extraction.

Conflicts of Interest: The authors declare no conflicts of interest.

References

1. Jia, J.; Hu, X.; Deng, Z.; Xiao, W.; Xu, H.; Han, F. Data-Driven Comprehensive Evaluation of Lithium-Ion Battery State of Health and Abnormal Battery Screening. *J. Mech. Eng.* **2021**, *57*, 141-149,159, doi:10.3901/JME.2021.14.141.
2. Feng, F.; Hu, X.; Hu, L.; Hu, F.; Li, Y.; Zhang, L. Propagation Mechanisms and Diagnosis of Parameter Inconsistency within Li-Ion Battery Packs. *Renew. Sustain. Energy Rev.* **2019**, *112*, 102–113, doi:10.1016/j.rser.2019.05.042.
3. Hu, X.; Zhang, K.; Liu, K.; Lin, X.; Dey, S.; Onori, S. Advanced Fault Diagnosis for Lithium-Ion Battery Systems: A Review of Fault Mechanisms, Fault Features, and Diagnosis Procedures. *IEEE Ind. Electron. Mag.* **2020**, *14*, 65–91, doi:10.1109/MIE.2020.2964814.
4. Jiang, X.; Jin, Y.; Zheng, X.; Hu, G.; Zeng, Q. Optimal Configuration of Grid-Side Battery Energy Storage System under Power Marketization. *Appl. Energy* **2020**, *272*, 115242, doi:10.1016/j.apenergy.2020.115242.

5. Hu, X.; Xu, L.; Lin, X.; Pecht, M. Battery Lifetime Prognostics. *Joule* **2020**, *4*, 310–346, doi:10.1016/j.joule.2019.11.018.
6. Hassan, A.; Khan, S.A.; Li, R.; Su, W.; Zhou, X.; Wang, M.; Wang, B. Second-Life Batteries: A Review on Power Grid Applications, Degradation Mechanisms, and Power Electronics Interface Architectures. *Batteries* **2023**, *9*, 571, doi:10.3390/batteries9120571.
7. Zhao, Q.; Liao, K.; Yang, J.; He, Z.; Xu, Y. Aging Rate Equalization Strategy for Battery Energy Storage Systems in Microgrids. *IEEE Trans. Smart Grid* **2023**, *PP*, 1–1, doi:10.1109/TSG.2023.3280226.
8. Xu, B.; Zhao, J.; Zheng, T.; Litvinov, E.; Kirschen, D. s Factoring the Cycle Aging Cost of Batteries Participating in Electricity Markets. *IEEE Trans. Power Syst.* **2017**, *PP*, doi:10.1109/TPWRS.2017.2733339.
9. Luo, Y.; Tian, P.; Yan, X.; Xiao, X.; Ci, S.; Zhou, Q.; Yang, Y. Energy Storage Dynamic Configuration of Active Distribution Networks—Joint Planning of Grid Structures. *Processes* **2023**, *12*, 79, doi:10.3390/pr12010079.
10. Yan, G.; Liu, D.; Li, J.; Mu, G. A Cost Accounting Method of the Li-Ion Battery Energy Storage System for Frequency Regulation Considering the Effect of Life Degradation. *Prot. Control Mod. Power Syst.* **2018**, *3*, doi:10.1186/s41601-018-0076-2.
11. Karunathilake, D.; Vilathgamuwa, D.; Mishra, Y.; Corry, P.; Farrell, T.; Choi, S.S. Degradation-Conscious Multiobjective Optimal Control of Reconfigurable Li-Ion Battery Energy Storage Systems. *Batteries* **2023**, *9*, 217, doi:10.3390/batteries9040217.
12. Collath, N.; Tepe, B.; Englberger, S.; Jossen, A.; Hesse, H. Aging Aware Operation of Lithium-Ion Battery Energy Storage Systems: A Review. *J. Energy Storage* **2022**, *55*, 105634, doi:10.1016/j.est.2022.105634.
13. Yu, C.; Zhu, J.; Liu, W.; Dai, H.; Wei, X. Co-Estimation of State-of-Charge and State-of-Temperature for Large-Format Lithium-Ion Batteries Based on a Novel Electrothermal Model. *Green Energy Intell. Transp.* **2024**, 100152, doi:10.1016/j.geits.2024.100152.
14. Xiao, W.; Xu, H.; Jia, J.; Feng, F.; Wang, W. State of Health Estimation Framework of Li-on Battery Based on Improved Gaussian Process Regression for Real Car Data. *IOP Conf. Ser. Mater. Sci. Eng.* **2020**, *793*, 012063, doi:10.1088/1757-899X/793/1/012063.
15. Liu, K.; Xiaopeng, T.; Teodorescu, R.; Gao, F.; Meng, J. Future Ageing Trajectory Prediction for Lithium-Ion Battery Considering the Knee Point Effect. *IEEE Trans. Energy Convers.* **2021**, *PP*, 1–1, doi:10.1109/TEC.2021.3130600.
16. Zhang, G.; Wei, X.; Tang, X.; Zhu, J.; Chen, S.; Dai, H. Internal Short Circuit Mechanisms, Experimental Approaches and Detection Methods of Lithium-Ion Batteries for Electric Vehicles: A Review. *Renew. Sustain. Energy Rev.* **2021**, *141*, 110790, doi:10.1016/j.rser.2021.110790.
17. Zheng, Y.; Lu, Y.; Gao, W.; Han, X.; Feng, X.; Ouyang, M. Micro-Short-Circuit Cell Fault Identification Method for Lithium-Ion Battery Packs Based on Mutual Information. *IEEE Trans. Ind. Electron.* **2021**, *68*, 4373–4381, doi:10.1109/TIE.2020.2984441.
18. Cui, Y.; Shen, X.; Zhang, H.; Yin, Y.; Yu, Z.; Shi, D.; Fang, Y.; Xu, R. Intrinsic Safety Risk Control and Early Warning Methods for Lithium-Ion Power Batteries. *Batteries* **2024**, *10*, 62, doi:10.3390/batteries10020062.
19. Xiao, W.; Miao, S.; Jia, J.; Zhu, Q.; Huang, Y. Lithium-Ion Batteries Fault Diagnosis Based on Multi-Dimensional Indicator. In Proceedings of the 2021 Annual Meeting of CSEE Study Committee of HVDC and Power Electronics (HVDC 2021); December 2021; Vol. 2021, pp. 96–101.
20. Zhao, J.; Gao, L.; Huang, B.; Yan, H.; He, M.; Jia, J.; Xu, H. Dynamic Monitoring of Voltage Difference Fault in Energy Storage System Based on Adaptive Threshold Algorithm. In Proceedings of the 2020 IEEE 4th Conference on Energy Internet and Energy System Integration (EI2); October 2020; pp. 2413–2418.
21. Zhang, K.; Hu, X.; Liu, Y.; Lin, X.; Liu, W. Multi-Fault Detection and Isolation for Lithium-Ion Battery Systems. *IEEE Trans. Power Electron.* **2022**, *37*, 971–989, doi:10.1109/TPEL.2021.3098445.
22. Doughty, D.H.; Crafts, C.C. *FreedomCAR :Electrical Energy Storage System Abuse Test Manual for Electric and Hybrid Electric Vehicle Applications.*; Sandia National Laboratories (SNL), Albuquerque, NM, and Livermore, CA (United States), 2006;
23. Białoń, T.; Niestrój, R.; Skarka, W.; Korski, W. HPPC Test Methodology Using LFP Battery Cell Identification Tests as an Example. *Energies* **2023**, *16*, 6239, doi:10.3390/en16176239.
24. Deng, Z.; Xiao, W.; Li, Y.; Huang, Y.; Jia, J.; Hu, X. Cycle Mileage Prediction of Electric Vehicle over Macro Timescale. *J. Mech. Eng.* **2021**, *57*, 250–258, doi:10.3901/JME.2021.24.250.
25. Wu, Z.; Yin, L.; Xiong, R.; Wang, S.; Xiao, W.; Liu, Y.; Jia, J.; Liu, Y. A Novel State of Health Estimation of Lithium-Ion Battery Energy Storage System Based on Linear Decreasing Weight-Particle Swarm

Optimization Algorithm and Incremental Capacity-Differential Voltage Method. *Int. J. Electrochem. Sci.* **2022**, *17*, 220754, doi:10.20964/2022.07.41.

26. Feng, X.; Merla, Y.; Weng, C.; Ouyang, M.; He, X.; Liaw, B.Y.; Santhanagopalan, S.; Li, X.; Liu, P.; Lu, L.; et al. A Reliable Approach of Differentiating Discrete Sampled-Data for Battery Diagnosis. *eTransportation* **2020**, *3*, 100051, doi:10.1016/j.etran.2020.100051.
27. Xiao, J.; Li, Q.; Bi, Y.; Cai, M.; Dunn, B.; Glossmann, T.; Liu, J.; Osaka, T.; Sugiura, R.; Wu, B.; et al. Understanding and Applying Coulombic Efficiency in Lithium Metal Batteries. *Nat. Energy* **2020**, *5*, 561–568, doi:10.1038/s41560-020-0648-z.
28. Severson, K.A.; Attia, P.M.; Jin, N.; Perkins, N.; Jiang, B.; Yang, Z.; Chen, M.H.; Aykol, M.; Herring, P.K.; Fraggedakis, D.; et al. Data-Driven Prediction of Battery Cycle Life before Capacity Degradation. *Nat. Energy* **2019**, *4*, 383–391, doi:10.1038/s41560-019-0356-8.
29. Wu, Z.; Jia, J.; Liu, Y.; Qi, Q.; Yin, L.; Xiao, W. Prediction of Battery Remaining Useful Life Based on Multi-Dimensional Features and Machine Learning. In Proceedings of the 2022 4th International Conference on Smart Power & Internet Energy Systems (SPIES); December 2022; pp. 1825–1831.
30. Zheng, Y.; Han, X.; Lu, L.; Li, J.; Ouyang, M. Lithium Ion Battery Pack Power Fade Fault Identification Based on Shannon Entropy in Electric Vehicles. *J. Power Sources* **2013**, *223*, 136–146, doi:10.1016/j.jpowsour.2012.09.015.
31. Wu, C.; Zhu, C.; Ge, Y. A New Fault Diagnosis and Prognosis Technology for High-Power Lithium-Ion Battery. *IEEE Trans. Plasma Sci.* **2017**, *45*, 1533–1538, doi:10.1109/TPS.2017.2706088.
32. Gateman, S.M.; Gharbi, O.; Gomes de Melo, H.; Ngo, K.; Turmine, M.; Vivier, V. On the Use of a Constant Phase Element (CPE) in Electrochemistry. *Curr. Opin. Electrochem.* **2022**, *36*, 101133, doi:10.1016/j.coelec.2022.101133.
33. Xiong, R.; Sun, Y.; Wang, C.; Tian, J.; Chen, X.; Li, H.; Zhang, Q. A Data-Driven Method for Extracting Aging Features to Accurately Predict the Battery Health. *Energy Storage Mater.* **2023**, *57*, 460–470, doi:10.1016/j.ensm.2023.02.034.
34. Zhang, K.; Xiong, R.; Qu, S.; Zhang, B.; Shen, W. Electrochemical Impedance Spectroscopy: A Novel High-Power Measurement Technique for Onboard Batteries Using Full-Bridge Conversion. *IEEE Trans. Transp. Electrification* **2024**, 1–1, doi:10.1109/TTE.2024.3362992.
35. Xiong, R.; Wang, S.; Feng, F.; Yu, C.; Fan, Y.; Cao, W.; Fernandez, C. Co-Estimation of State-of-Charge and State-of-Health for High-Capacity Lithium-Ion Batteries. *Batteries* **2023**, *9*, 509, doi:10.3390/batteries9100509.
36. Xiong, R.; Wang, S.; Huang, Q.; Yu, C.; Fernandez, C.; Xiao, W.; Jia, J.; Guerrero, J.M. Improved Cooperative Competitive Particle Swarm Optimization and Nonlinear Coefficient Temperature Decreasing Simulated Annealing-Back Propagation Methods for State of Health Estimation of Energy Storage Batteries. *Energy* **2024**, *292*, 130594, doi:10.1016/j.energy.2024.130594.
37. Jia, X.; Wang, S.; Cao, W.; Qiao, J.; Yang, X.; Li, Y.; Fernandez, C. A Novel Genetic Marginalized Particle Filter Method for State of Charge and State of Energy Estimation Adaptive to Multi-Temperature Conditions of Lithium-Ion Batteries. *J. Energy Storage* **2023**, *74*, 109291, doi:10.1016/j.est.2023.109291.
38. Gu, Y.; Chen, Y.; Wang, J.; Xiao, W.; Chen, Q. Enhancing Dispatchability of Lithium-Ion Battery Sources in Integrated Energy-Transportation Systems With Feasible Power Characterization. *IEEE Trans. Ind. Inform.* **2023**, *19*, 1997–2007, doi:10.1109/TII.2022.3195731.
39. Liu, W.; Hu, X.; Lin, X.; Yang, X.-G.; Song, Z.; Foley, A.M.; Couture, J. Toward High-Accuracy and High-Efficiency Battery Electrothermal Modeling: A General Approach to Tackling Modeling Errors. *eTransportation* **2022**, *14*, 100195, doi:10.1016/j.etran.2022.100195.
40. Xiong, R.; Wang, S.; Yu, C.; Fernandez, C.; Xiao, W.; Jia, J. A Novel Nonlinear Decreasing Step-Bacterial Foraging Optimization Algorithm and Simulated Annealing-Back Propagation Model for Long-Term Battery State of Health Estimation. *J. Energy Storage* **2023**, *59*, 106484, doi:10.1016/j.est.2022.106484.
41. Gu, Y.; Wang, J.; Chen, Y.; Xiao, W.; Deng, Z.; Chen, Q. A Simplified Electro-Chemical Lithium-Ion Battery Model Applicable for in Situ Monitoring and Online Control. *Energy* **2022**, doi:10.1016/j.energy.2022.126192.
42. Luo, G.; Zhang, Y.; Tang, A. Capacity Degradation and Aging Mechanisms Evolution of Lithium-Ion Batteries under Different Operation Conditions. *Energies* **2023**, *16*, 4232, doi:10.3390/en16104232.
43. Naylor Marlow, M.; Chen, J.; Wu, B. Degradation in Parallel-Connected Lithium-Ion Battery Packs under Thermal Gradients. *Commun. Eng.* **2024**, *3*, 1–15, doi:10.1038/s44172-023-00153-5.

 doi:10.20944/preprints202403.1129.v1

44. Liu, K.; Shang, Y.; Ouyang, Q.; Widanage, W. A Data-Driven Approach With Uncertainty Quantification for Predicting Future Capacities and Remaining Useful Life of Lithium-Ion Battery. *IEEE Trans. Ind. Electron.* **2020**, *PP*, 1–1, doi:10.1109/TIE.2020.2973876.
45. Fan, T.-E.; Liu, S.-M.; Yang, H.; Li, P.-H.; Qu, B. A Fast Active Balancing Strategy Based on Model Predictive Control for Lithium-Ion Battery Packs. *Energy* **2023**, *279*, 128028, doi:10.1016/j.energy.2023.128028.